ELSEVIER

Remote Sensing of Environment

Large-Scale BRDF Retrieval over New Mexico with a Multiangular NOAA AVHRR Dataset

*Mark J. Chopping**

In this study a number of linear semiempirical kernel-driven (LiSK) bidirectional reflectance distribution function (BRDF) models are adjusted against an extensive Advanced Very High Resolution Radiometer (AVHRR) dataset collected over a variety of semiarid cover types in the southern part of New Mexico and parts of Chihuahua, Mexico as part of the May 1997 Prototype Validation Exercise (PROVE) campaign, an activity of the NASA Earth Observing System Terra validation program. The aim is to investigate model behavior under conditions of sparse angular sampling such as that provided by the AVHRRs and MODIS over a wide variety of southwestern desert surface types. Linear semiempirical models of the type to be used in the MODIS/MISR BRDF/albedo product (MOD43) are inverted, since these are appropriate for use over large areas. The results of the inversions show that these models are able to describe BRDF for a wide variety of surfaces and provide both a means for correcting for directional phenomena in satellite data and for extracting structural information from multiangular reflectance datasets. Published by Elsevier Science Inc.

INTRODUCTION

As part of the Prototype Validation Exercise (PROVE) campaign, an activity of the NASA Earth Observing System Terra-1 validation program, 22 High Resolution Picture Transmission (HRPT) datasets from the NOAA Advanced Very High Resolution Radiometers (AVHRR) on the NOAA-12 and NOAA-14 satellites corresponding to the campaign period were acquired, georeferenced, and calibrated to percent albedo by researchers at the University of Colorado. Subsets of these data have been used in other studies as a means of investigating variations in the bidirectional reflectance distribution function (BRDF) and albedo at the grassland and grassland-mesquite transition sites within the United States Department of Agriculture Agricultural Research Service (USDA-ARS) Jornada Experimental Range (Hyman et al., 1998; Barnsley et al., 2000) and of validating geometric-optical and radiative transfer (GORT) BRDF models (Ni and Li, 2000).

In this study a number of linear semiempirical kernel-driven (LiSK) BRDF models are adjusted against these AVHRR data, with the focus on kernel combinations using the LiSparse surface geometric-optical kernels with either the RossThin or the RossThick volume scattering kernel. The models are derived in Wanner et al. (1995) and are based on the formulation of Roujean et al. (1992b); detailed descriptions will not be given here. These models have been suggested as part of a multimodel algorithm for MODIS BRDF processing (Strahler et al., 1996). The aim is to investigate model behavior under conditions of sparse angular sampling (as provided by the AVHRRs) over the southern part of New Mexico and parts of Chihuahua, Mexico. This area encompasses both the USDA-ARS Jornada Experimental Range (JER) and the Sevilleta National Wildlife Refuge (NWR) and a wide range of cover types, including desert grassland, semiarid grassland, grassland-shrub transition, desert shrubland, forest, dry lake bed, alkali flats, and the gypsum dunes of White Sands National Monument, among others. LiSK models are appropriate for use over large areas (since they are rapidly inverted) and can be used with sparse angular datasets (since the small number of parameters tends to lead to robust retrievals). They are particularly appropriate for use with AVHRR data over arid and semiarid regions where cloud cover is not prohibitive. The ability to account for BRDF effects in AVHRR Channel 1 (visible) and 2 (near-infrared) data is important since many researchers have recognized limitations with these multiangular data when uncorrected (Roujean et al., 1992a; Goward et al., 1993; Kremer and

* USDA-ARS Hydrology Laboratory, Beltsville Agricultural Research Center-West, Beltsville, Maryland

Address correspondence to Mark J. Chopping, USDA-ARS Hydrology Lab., Beltsville Agricultural Research Ctr.-West, Beltsville, MD 20705-2350. E-mail: chopping@hydrolab.arsusda.gov

Received 15 July 1999; revised 20 August 1999.

REMOTE SENS. ENVIRON. 74:163–191 (2000)
Published by Elsevier Science Inc.
655 Avenue of the Americas, New York, NY 10010

0034-4257/00/$–see front matter
PII S0034-4257(00)00120-6

Running, 1993; Cabot et al., 1994; Cihlar et al., 1994a,b; Moody and Strahler, 1994; Bastin et al., 1995, Meyer et al., 1995; Wu et al., 1995; Zhu and Yang, 1996; Burgess and Pairman, 1997). Accounting for BRDF effects and extracting structural information allows important improvements in cover classifications (LeRoy and Bréon, 1996; Chopping 1998a,b,c) and the retrieval of albedo and other bio- and geophysical parameters (Privette et al., 1996; Asner et al., 1998; Hyman et al., 1998).

Inversion of explicit models is necessary because BRDF is dynamic in space and time, and it is not feasible to apply corrections for directional phenomena which are based on simple interpolation or extrapolation (Los et al., 1995; Chopping, 1999), or brightness adjustments (Jupp et al., 1994). In spite of the theoretical advantages of linear BRDF models over other methods in correcting for BRDF effects in coarse multiangular data such as that from the AVHRR, the science community has been slow to realize their potential. This is partly because the AVHRR has not been regarded as a multiangular sensor, in spite of the relatively wide range of sun and viewing geometries provided (Barnsley et al., 1994). It is also partly because early attempts to use linear BRDF models to correct for directional effects in AVHRR data have not always been wholly successful, sometimes owing to misunderstandings of the application of the models. For example, Burgess and Pairman (1997) evaluated the empirical Walthall model (Walthall et al., 1985) with AVHRR data from NOAA-11 (PM) and found good fits to the model but went on to state that this approach is impractical because "the model fits are channel- and land cover type-dependent." However, it should be self-evident that BRDF is dynamic spatially, spectrally and temporally. Wu et al. (1995) were also concerned with the dependence of BRDF on broad land cover type; they proceeded by fitting the Roujean model (Roujean et al., 1992b) against reflectance data for specific land cover categories and then adjusting the retrieved parameters by reference to first- and second-order relationships with the normalized difference vegetation index (NDVI). It is not clear why this approach was chosen rather than inverting the model directly for all observations individually; it is known that NDVI is suboptimal for some environments—particularly sparse, discontinuous semiarid canopies (Huete et al., 1994)—and that BRDF is dynamic, changing within land cover types (Brown de Colstoun et al., 1996; Hyman and Wanner, 1997; Lewis et al., 1998). Even quite recently some workers have expressed the opinion that LiSK models are costly in terms of computational demand and require a large number of input variables, although both claims are clearly incorrect (Chopping, 1999). Very recent work using a 3-D scene modeling system has shown that one of the major assumptions made in the LiSK model formulation—that bidirectional reflectance may be decomposed as a sum of contributions from different scene components—does hold for instruments with fields-of-view much larger than the scale of surface features

Table 1. AVHRR Overpasses: Times, Geometries, and Atmospheric Conditions Assumed for Retrieval of Surface Reflectance with the SMAC Algorithm

Filename[a]	*Local Time*	*View Zenith (°)*		*Solar Zenith (°)*		*Relative Azimuth*[c] *(°)*	*Water Vapor (g/cm²)*	*Aerosol Optical Thickness at 550 nm*[d]
		Min[b]	*Max*	*Min*	*Max*			
n14_970510_2125	15:25	30	58	33	39	9	1.8317	0.0936
n12_970513_1344	7:44	0	34	67	73	19	1.4569	0.0793
n14_970513_2052	14:52	0	26	26	32	168	1.6055	0.1159
n12_970514_1323	7:23	24	56	72	77	18	1.4062	0.0723
n12_970515_1441	8:41	50	70	55	60	160	1.4062	0.0723
n12_970517_1357	7:57	0	36	64	70	160	1.4862	0.0835
n14_970525_2021	14:21	28	60	17	24	163	1.1455	0.0652
n12_970527_1338	7:38	0	40	67	73	22	0.8661	0.0520
n12_970528_0059	18:59	0	41	75	81	150	0.9075	0.0413
n12_970528_1316	7:16	34	60	72	78	22	1.3970	0.0710
n14_970528_2129	15:29	33	60	31	37	4	1.3719	0.0881
n14_970529_2118	15:18	17	51	29	35	4	1.1238	0.1468
n12_970530_1412	8:12	14	53	60	66	157	1.1960	0.0619
n12_970531_1350	7:50	0	27	65	70	157	2.3303	0.1282
n14_970531_2056	14:56	0	26	24	30	6	2.4538	0.1773
n12_970601_1328	7:28	13	50	69	75	22	1.4187	0.0740
n14_970601_2045	14:45	0	37	21	28	173	1.6166	0.1170
n12_970602_0049	18:49	11	51	73	79	150	0.9629	0.0488
n12_970602_1306	7:06	45	66	73	79	22	1.3623	0.0663
n14_970602_2034	14:34	10	49	20	26	173	1.6332	0.1185
n12_970603_0027	18:27	42	66	68	74	149	1.0443	0.0576
n12_970603_1424	8:24	33	62	57	63	156	1.0443	0.0576

[a] Excluding cloud cover and channel indicators: nSatID_YYMMDD_HHMM (GMT).
[b] Rounded to nearest value; zero implies that the subsatellite track is in the subscene.
[c] Relative azimuths (φ) given are approximate (see Fig. 1); note that where minimum view zeniths are zero, relative azimuths are likely to include $180 \pm \varphi$.
[d] Ozone set at 0.189 cm-atm; ground pressure set at 1013.25 hPa (the only valid value).

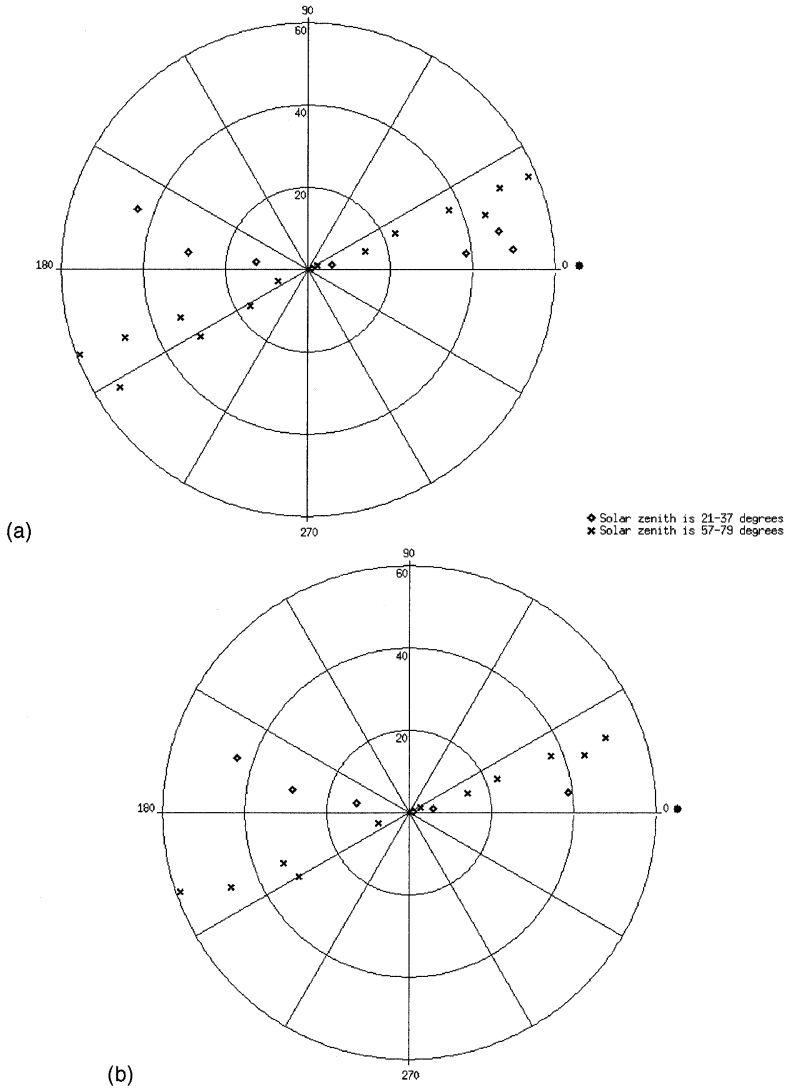

Figure 1. The angular sampling provided by AM/PM AVHRRs for the western Sevilleta creosote site (see Table 6) for 10 May–3 June 1997: a) without screening for cloud and shadow; b) with screening. Distance from the center defines view zenith and the radial axis defines the azimuthal orientation of the observations, with the Sun located at 0° (i.e., backscattering in the rightmost quadrants). Note that these data are representative but do not include all possible acquisitions for this period.

such as shrubs (Qin and Gerstl, 2000). This work follows similar research into the operation of LiSK models with 3-D modeling and Monte Carlo ray tracing which showed that some physical meaning is retained in LiSK model parameters (kernel weights), even though some biophysical parameters are coupled (Lewis and Disney, 1997). Inversion of LiSK models with data from satellite altitudes has proved more difficult to effect successfully, however.

The first attempt to calibrate a LiSK BRDF model with AVHRR data for BRDF correction used an 8-month dataset (March–October 1989) composed of daily LAC data from the AVHRR on the NOAA-11 (PM) satellite over a number of test sites in France (Leroy and Roujean, 1994). The authors developed a sliding window technique over a period of 30 days, during which surface properties are assumed stationary, with data from each 30-day window used to calibrate the Roujean model. They showed that model fits to observations were good and that series of modeled reflectances (the isotropic parameter) do not exhibit the large short-term fluctuations associated with bidirectional effects evident in the uncorrected series, resulting in lower standard deviations and more reasonable temporal trajectories. They estimated that noiselike fluctuations in the observed series of reflectances were reduced by a factor of up to 3, with larger reductions where noise in the observed data was large. Privette and Vermote (1995) carried out an evaluation of a variety of LiSK models against atmospherically corrected visible wavelength reflectances derived from Global Area Coverage (GAC) data from NOAA-11 (PM) acquired in early March 1993 over a desert in North Africa. They found that reasonably good fits were found for three-kernel models (mean RMSE of 0.034 for an isotropic-LiSparseLO–RossThin model against 0.015 for the nonlinear six-parameter SOILSPECT model). Note that the LiSK models are formulated with the assumption of sparse to dense vegetation rather than the very low vegetation quantities likely in this true desert region.

Recently LiSK models have been inverted for the entire globe (Zhang et al., 1998) and at continental scales (Kalluri et al., 1997) with 8 km resolution data from the

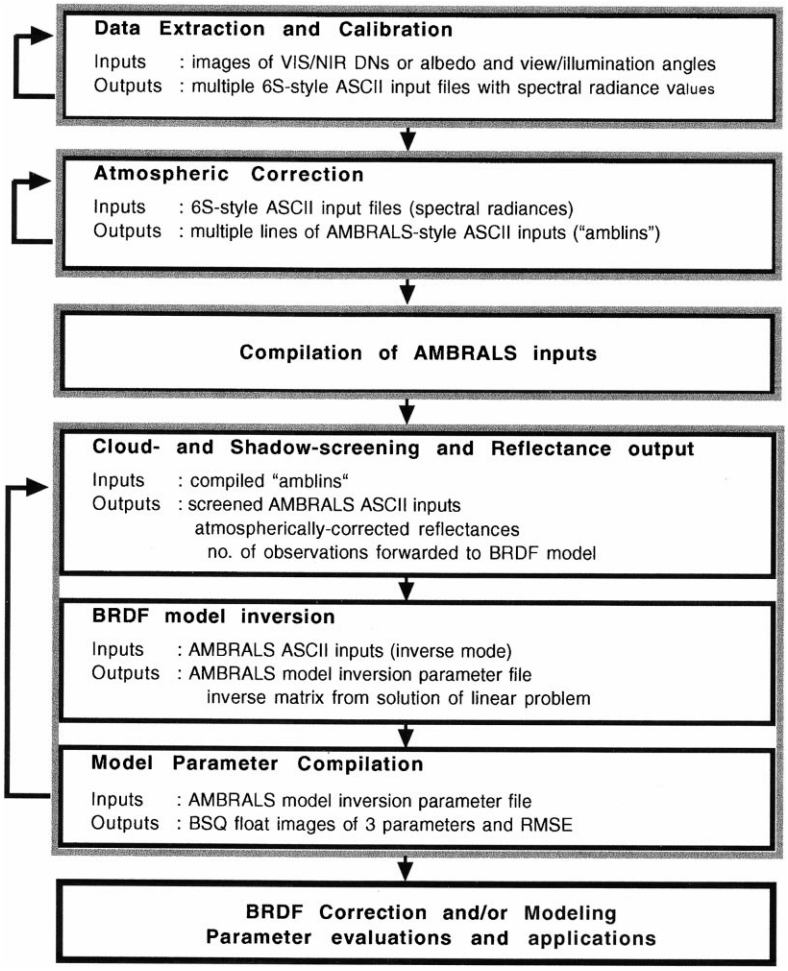

Figure 2. Overview of processing for BRDF correction and modeling. Arrows indicate iteration over multiple samples (locations).

Pathfinder Land (PAL) AVHRR dataset, although parameter retrievals may be unstable since the angular range of the directional reflectance inputs is limited: only data from the AVHRR on the PM satellite are used so the variation in solar zenith angles will be small. Furthermore, since global BRDF retrieval was the aim, observations must be collected over periods much longer than that in which important changes in vegetation status might be expected. O'Brien et al. (1998) used full resolution AVHRR data from NOAA-14 to invert the the semiempirical LiSparse geometric-optical model over very sparsely-vegetated sites; again only data from the PM sensor were used. In addition, no corrections for atmospheric scattering or absorption were effected; model inversion was necessarily by numerical methods—since the LiSparse kernel's internal parameters are left free—and no volume scattering kernel was included. Vives Ruiz de Lope and Lewis (1997) carried out an extensive evaluation of the behavior of the Algorithm for MODIS Bidirectional Reflectance Anisotropies of the Land Surface (AMBRALS) algorithm (selection from a variety of kernel combinations) over three HAPEX Sahel supersites (tiger bush, millet, and fallow), which is one of the few studies to have used data from both AM and PM AVHRR sensors (with calibration based on ground targets; see also Privette et al., 1996). They found that the RossThin kernel provided the lowest root-mean-square error (RMSE) for the majority of locations and conclude that LiSK models perform well in normalizing reflectance data for directional effects with temporal parameter trajectories providing information additional to that provided by traditional (i.e., uncorrected) NDVI profiles.

METHOD

Data

The AVHRR observations used are from 22 overpasses which fall within a 33-day period from 10 May to 3 June 1997. This period corresponds to the end of the dry season and is relatively long in relation to the planned 16-day production cycle of the MODIS BRDF/albedo product (Strahler et al., 1996). Just over half of the scenes are from the AVHRR on the NOAA-12 (AM) satellite but note that three scenes from this sensor were acquired in the evening (see Table 1). In order to invert BRDF models using AVHRR data, the assumption is made that surface conditions do not change importantly over the data acquisition period. After cloud and shadow contamination, BRDF effects and changes in vegetation status as a result of fire, the most important source of variation in surface reflectance

estimates is likely to be changes from dry to wet soil following rainfall. The Jornada Long-Term Ecological Research (LTER) weather station database shows that there was little rainfall during this period at the JER (26.7 mm) with only two relatively big events: 9.4 mm on the evening of the 10 May, after the PM overpass and 13.5 mm on the evening of 19 May which would not affect the next acquisition (25 May). For the Sevilleta NWR there were only two notable events in this period : 1.5 mm and 7.3 mm on 15 and 20 May, respectively.

The objective is to provide the BRDF models with the maximum number of valid (contamination-screened) surface reflectance estimates for each location, with the greatest possible variation in view and illumination geometry (i.e., the best angular sampling available). In order to avoid the need to calculate the Sun–sensor geometry in real time within the processing chain, grids of view and solar zeniths and azimuths were created for each AVHRR overpass, of the same dimensions and in the same projection as the Channel 1 and 2 data. A typical angular sampling régime is shown in Figure 1; it can be seen that the observations lie close to the principal plane with greater azimuthal variation in the forward-scattering half-space. The ranges of viewing and solar zeniths are 0–59° and 21–79°, respectively; in terms of sampling the BRDF this is sparse and lacks observations at a hot spot geometry. On the other hand, the most important variation in BRDF is located close to the principal plane and the directional reflectance signal is captured for a large range of Sun angles. Note that the models obey the Helmholtz reciprocity principle whereby Sun and viewing positions may be exchanged.

Multiscene AVHRR Processing Algorithm: Overview

In order to minimize the time taken to invert BRDF models for a large number of locations, the processing is organized as a series of processes each with responsibility for a user-defined subset of the total image (in this case 50 rows for 480 columns), making concatenation of the results to form complete images straightforward. This block-based approach enables processing from the extraction of albedo and Sun–sensor geometry to BRDF model inversions to complete very rapidly (~4 h 30 min for the 491×480 region—235,680 cells—on a 450 MHz Pentium II processor running Linux). The inversions are effected here with the Algorithm for MODIS Bidirectional Reflectance Anisotropies of the Land Surface (AMBRALS) code, version 2.4 (Strahler et al., 1996), corrected for an error in the calculation of relative azimuths. This code solves the set of linear equations defining the minimum of the error function chosen to measure the difference between modeled and observed values; this is a matrix inversion problem and is performed using LU decomposition with absolute values in the error function (mean square absolute deviation):

$$\delta^2 = \frac{\sum(\rho_{\text{mod}} - \rho_{\text{obs}})^2}{n}, \quad (1)$$

where ρ_{mod} is the modeled bidirectional reflectance, ρ_{obs} is the observed value, n is the number of observations and δ^2 is the residual to minimize. Note that no kernel selection is performed here; only one combination of kernels ("model") is inverted at a time.

A graphical overview of the processing chain is given in Figure 2. Demands on processor time and storage are important since the input data—calibrated albedo and view and illumination geometry from all 22 overpasses for two channels—must be available simultaneously for each location. The processing stages required to provide the required set of observations for one location and for all overpasses are:

1. extraction of channel albedo and observation geometry;
2. recalibration of albedo to units of spectral radiance;
3. calculation of TOA (apparent) reflectance and retrieval of surface reflectance estimates via atmospheric correction.

These operations result in 44 files, one per overpass per channel, which are subsequently concatenated together to provide multiple series of 22 candidate inputs (reflectance and geometry) for each channel. The two sets of series are screened for extreme and anomalous values resulting from line dropouts, noise spikes, cloud and cloud-shadow; and the number of valid clear-to-surface observations are counted. This is a critical point since the forwarding of contaminated observations to the BRDF model will severely compromise inversions. The remaining stages in processing are:

4. screening for valid surface observations and compilation of the final AMBRALS input file;
5. submission of the two input files to the AMBRALS software for model inversion; and
6. extraction from the AMBRALS ASCII output file of the three model parameters and RMSE obtained for the current sample. These are appended to binary files, so that subimages of parameters and RMSE are accumulated.

Stage 4 additionally writes images of the number of valid observations to be used in model inversion and the atmospherically corrected channel reflectances, tagged by sign to indicate invalid observations (i.e., negative, extreme or contaminated by cloud or cloud-shadow). Stage 5 also writes the 3×3 inverse matrix used in solving the inversion problem (see Lewis and Wanner, 1996). The first version of the algorithm operated on a sample-by-sample basis, but this is extremely slow and results in proliferation of very shortlived processes; operating on blocks of samples increases processing speed by a factor of 20 and is easily accomplished by iterating stages 1–3 above and then sub-

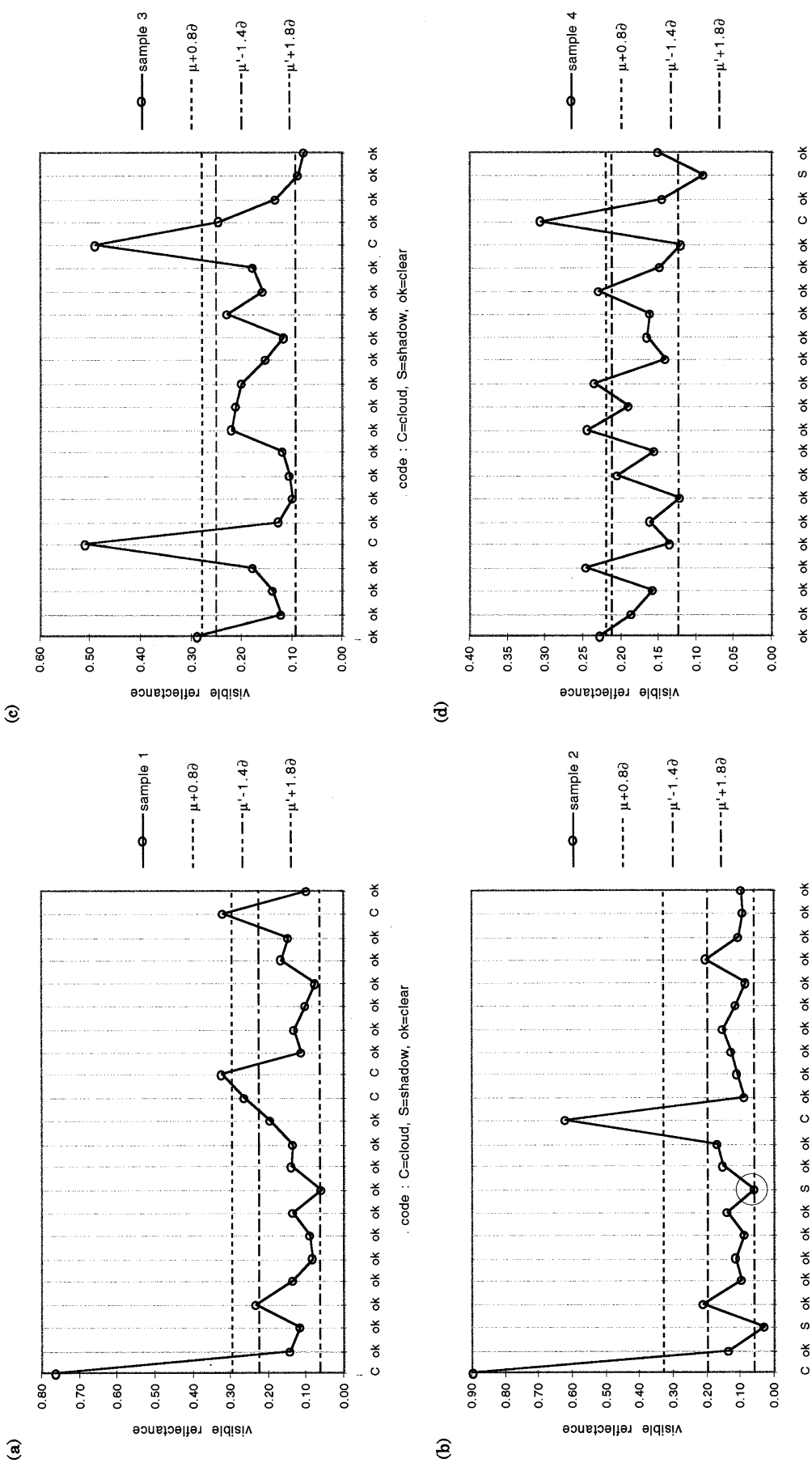

Figure 3. Contamination screening via decomposition of variability in AVHRR Channel 1 reflectance series. Samples selected to include cloud and/or shadow. Primes (μ') indicate a mean calculated from a pre-screened series (see text).

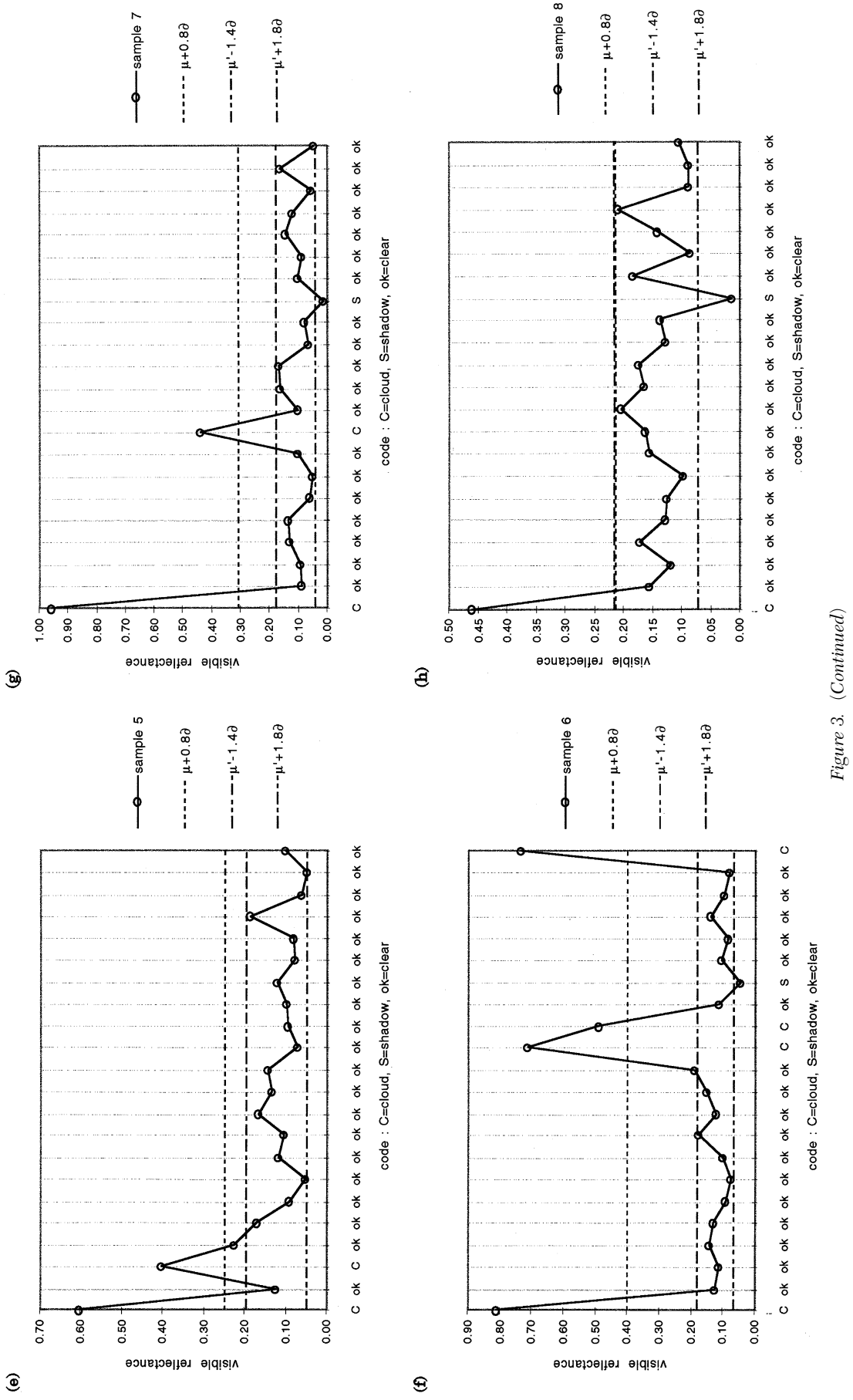

Figure 3. (Continued)

mitting the multiple outputs to stages 4–6. Note that in providing the following detailed descriptions the intention is not to advocate this particular set of methods for operational processing but to fully and carefully report what was done.

Multiscene AVHRR Processing Algorithm: Details

There are four major considerations in the design of the processing chain: precision, speed, storage, and flexibility. The processing is decomposed into several well-defined steps in order to maintain as much flexibility as possible and to aid in testing. For example, calibrated spectral radiance in units of W m^2 μm^{-1} sr^{-1} written by the data extraction program may be presented to either 6S (Second Simulation of the Satellite Signal in the Solar Spectrum, Vermote et al., 1997) or to a modified SMAC (Simplified Method for Atmospheric Correction) algorithm (Rahman and Dedieu, 1994). Likewise, it is straightforward to replace the AMBRALS BRDF/albedo modeling software with other modeling packages; only minor modifications to the code are required.

Post-Launch Calibration

In the implementation of each processing stage decisions are made which could impact severely on BRDF model inversions; the most important of these concern calibration, atmospheric correction and screening for contamination. It is well known that the responses of the visible and near-infrared channel detectors of all AVHRR sensors degrade rapidly after launch as a result of outgassing and other stresses, subsequently degrading more gradually over time (Rao and Chen, 1993; Rao and Chen, 1996). This means that the prelaunch calibration coefficients very quickly become inadequate and with no onboard calibration other techniques have had to be devised in order to inter-calibrate among different sensors and over long periods of time. These techniques include comparisons with contemporaneous aircraft underflights and ground observations with the selection of radiometrically stable surface targets such as the Southern Libyan desert (Rao and Chen, 1996) and the ice caps (Loeb, 1997).

For this study, calibration for the NOAA-14 AVHRR was based on formulae given by Rao and Chen (1999; NOAA-NESDIS Office of Research and Applications) and which include a degradation factor based on days since launch:

$$\text{Ch. 1 slope} = (0.000690d + 0.566)\cdot((C_{10} - 41)e),$$

$$\text{Ch. 2 slope} = (0.000435d + 0.440)\cdot((C_{10} - 41)e),$$

where d is days since launch, C_{10} is the 10-bit channel digital number (DN), and e is a multiplicative factor to normalize the offset digital number (DN) to mean Earth–Sun distance.

For the NOAA-12 AVHRR there are no post-launch Channel 1 and 2 coefficients corresponding to the study period; the last updates were published by Loeb (1997) for summer and winter 1994 and 1995. There is a very slight and consistent trend in summer and winter values over these two years and in the absence of more recent updates temporal extrapolation to summer 1997 is reasonable in view of both seasonal and long-term trends in coefficient values; Loeb found that changes in coefficients over the period June 1994 to December 1995 were small and less than the uncertainty in the derived coefficients. Note that the new values obtained by Loeb are 20% and 35% greater than the prelaunch values for Channels 1 and 2, respectively; the prelaunch values are clearly completely inadequate. For both AM and PM sensors, calibration does not take into account the effects of the sensor point spread function (disproportionate contribution of different areas under the instrument field-of-view changing with view zenith angle).

Atmospheric Corrections

Retrieval of surface reflectance ("atmospheric correction") is extremely important to surface BRDF retrieval. Even with a clean atmosphere (i.e., low aerosol concentrations) molecular scattering and absorption have an impact which varies with path length, ozone, and water vapor concentrations. Note that the atmosphere is not a Lambertian scatterer and has its own BRDF (Rahman, 1996). The processing effected here uses the Simplified Method for Atmospheric Correction (SMAC) algorithm, which is based on the 5S code with maximum deviations from 5S of ~2.35% and ~3.11% reflectance in the AVHRR visible and near-infrared channels, respectively (Rahman and Dedieu, 1994). The code executes almost 1325 times faster than 5S. Since SMAC requires TOA (apparent) reflectance as input rather than spectral radiance it was necessary to convert the latter to units of reflectance. This is achieved by

$$\rho^* = \frac{L}{E_s \cdot d \cdot \cos(\theta_s)}, \tag{2}$$

where L is the calibrated spectral radiance from the sensor (W m^2 μm^{-1} sr^{-1}), E_s is the in-band equivalent solar radiance at the mean Earth–Sun distance (W m^2 μm^{-1} sr^{-1}), d is a multiplicative factor used to account for variations in the solar constant with season, $\cos(\theta_s)$ is the cosine of the solar zenith angle, and ρ^* is apparent reflectance at the top of the atmosphere (dimensionless). The factor used to account for variations in the solar constant, d, is calculated from

$$d = \frac{1}{(1 - e\cos M)^2} \tag{3}$$

with

$$M = 0.9856(J - 4)(\pi/180), \tag{4}$$

where $e = 0.01673$ and J is the Julian day of the year (see the VARSOL routine of 6S, Vermote et al., 1997). SMAC is provided with atmospheric parameters from measurements of water vapor, ozone, and aerosol optical thickness

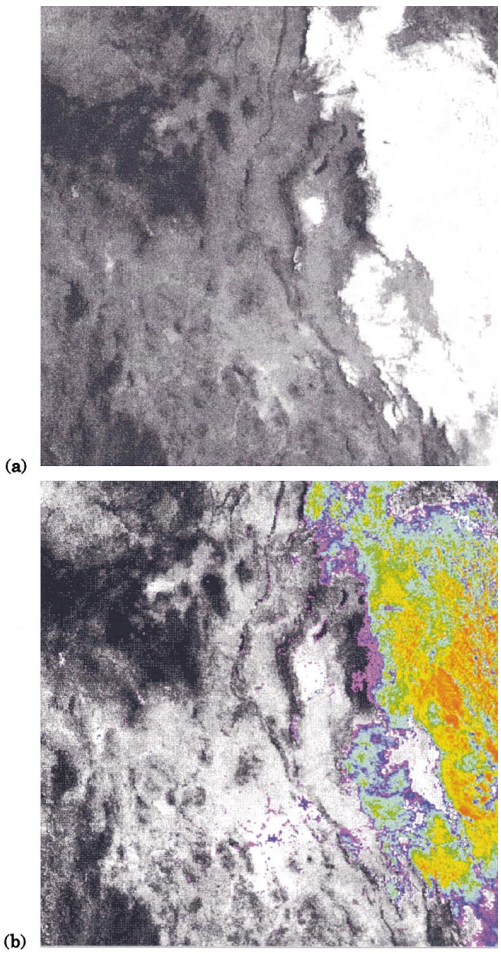

Figure 4. NOAA-12 Subscene 31 May 13:50 GMT Channel 1: a) DNs; b) reflectance flagged for contamination (ROYGBIV scale from high to low values; red is cloud; violet is shadow).

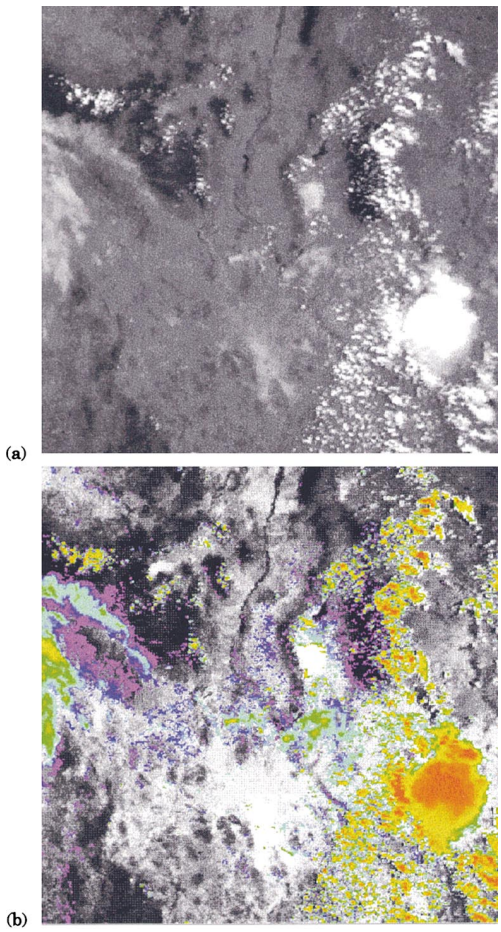

Figure 5. NOAA-14 Subscene 28 May 21:29 GMT Channel 1: a) DNs; b) reflectance flagged for contamination (ROYGBIV scale from high to low values; red is cloud; violet is shadow).

(τ) collected by various investigators as part of the Grassland PROVE campaign. Note that these parameters were acquired at the Jornada Experimental Range but that ground pressure is set to a value of 1013.25 (the only valid value in this version of SMAC). In order to calculate aerosol optical thickness at 550 nm (τ550), τ440 and τ675 data from CIMEL sun photometers at the nearest time to the overpasses—and always within 5 minutes—were used with the Angstrom coefficient. A second-order equation based on time-of-day was used to interpolate for cases where CIMEL data were absent for a particular day; a similar strategy was adopted for water vapor, except there is no spectral dependence. These values were provided by J. L. Privette (NASA-GSFC). A single ozone value was provided by K. Thome (Remote Sensing Group, University of Arizona) based on the cleanest data set, since values do not vary much in nature over short periods. Note that this atmospheric correction scheme may be deemed a Lambertian-based correction, since no account is taken of the surface BRDF and there is no surface-atmosphere coupling.

Contamination Screening

From the point of view of providing directly illuminated clear-to-surface observations to the BRDF model, the major sources of contamination in the channel data are cloud cover and cloud shadow. Much research has been carried out and published on the subject of detection and screening of cloud cover in AVHRR scenes, often in the context of producing near cloud-free multiorbit composites (Holben, 1986; Cihlar et al., 1994a,b). This research has led to the development of tests varying in their sophistication and complexity based on apparent temperature, spatial consistency over small image windows, visible and near-infrared channel thresholds, and neural network training (Kwiatowska 1995). The NOAA/NASA 8 km Pathfinder Land and EROS-EDC-USGS 1 km AVHRR Land programs have both adopted the maximum value compositing with NDVI (MVCN) criterion for the production of 10-day composites, a criterion advocated by Holben (1986) on the basis of simulated AVHRR data and which is generally considered as a standard processing method. The MVCN compositing criterion has been critically evaluated by Cihlar et al. (1994)

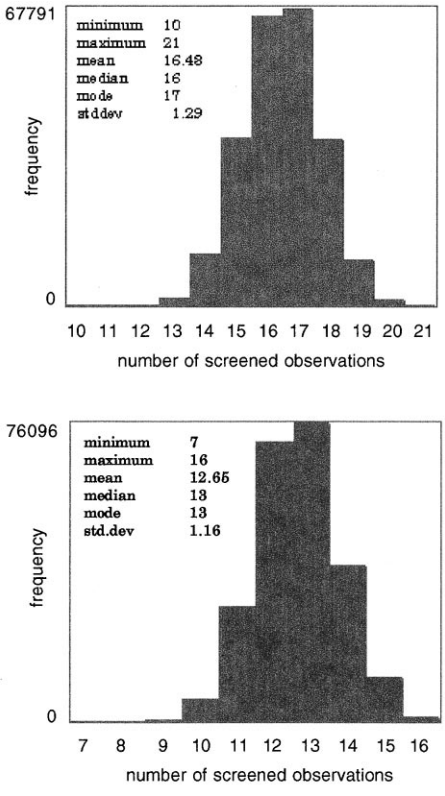

Figure 6. Frequency distribution and statistics for grids of observations available per location for the 33-day period a) using all 22 overpasses and b) using only 17 overpasses (see Table 3).

against a number of alternative criteria and found to be a relatively poor choice; similar conclusions are drawn by Moody and Strahler, (1994), Goetz (1997), Vives Ruiz de Lope and Lewis (1997), Stoms et al. (1997), and Gallo and Huang (1998). In spite of its widespread adoption and continued use by the science community (e.g., Marçal and Wright, 1997), the MVCN criterion is clearly inadequate in a number of important respects. First, it does not take the BRDF characteristics of land surfaces into account and over humid regions preferentially selects observations in the forward direction rather than close to nadir; this is the behavior which would be expected on the basis of observed BRDFs in the visible and near-infrared wavelengths. This leads to directional artifacts in MVCN composites which are not insignificant; a study to evaluate data quality for a North American subset of the 1 km AVHRR Land reprocessing found a strong bias in the distribution of angular values (Zhu and Yang, 1996). Second, it was discovered in the course of developing the contamination screening for processing a similar AVHRR dataset over Inner Mongolia (P. R. China) that it is possible for shadowed observations to produce NDVIs which are higher than those of temporally adjacent clear observations, even over a 17-day period and for both AM and PM satellites (Chopping, 1998c).

In spite of the long history of working with AVHRR

Table 2. Root-Mean-Square Error Image Statistics (Expressed as % Reflectance) on Fitting Various Linear BRDF Models to Surface Reflectance Estimates from All 22 AVHRR Orbits and a Reduced Set of 17 Orbits (see Table 3)[a]

Model:	*LSRn*	*LSRk*	*Rou*	*mW*	*LSRn*	*LSRk*	*Rou*	*mW*	*LSRn*	*LSRk*	*Rou*	*mW*	*LSRn*	*LSRk*	*Rou*	*mW*
# Orbits:	*17*	*17*	*17*	*17*	*22*	*22*	*22*	*22*	*17*	*17*	*17*	*17*	*22*	*22*	*22*	*22*
Channel:	*VIS*	*VIS*	*VIS*	*VIS*	*VIS*	*VIS*	*VIS*	*VIS*	*NIR*	*NIR*	*NIR*	*NIR*	*NIR*	*NIR*	*NIR*	*NIR*
Min	0.3	0.2	0.2	0.2	0.7	0.7	0.6	0.6	0.5	0.3	0.3	0.4	0.8	0.7	0.4	0.6
Max	15.8	15.7	15.7	16.5	14.9	14.8	14.5	14.5	14.0	13.8	1.38	14.4	14.4	14.9	14.4	13.5
Mean	2.9	2.8	2.8	2.8	3.1	3.2	3.1	2.9	3.3	3.3	3.3	3.1	3.9	4.1	3.1	3.4
Median	2.5	2.5	2.5	2.5	2.9	2.9	2.8	2.6	3.0	3.0	3.0	2.8	3.7	3.9	2.8	3.2
Mode	1.9	1.9	1.9	1.9	2.7	2.6	2.6	2.3	2.6	2.5	2.5	2.5	3.3	3.6	2.5	2.7
St. dev.	1.5	1.4	1.4	1.4	1.1	1.1	1.1	1.1	1.3	1.3	1.3	1.3	1.1	1.2	1.3	1.2

[a]Models are isotropic kernel (unity) plus LS=LiSparseMODIS, Rn=RossThin, Rk=RossThick, Rou=Roujean model). mW=modified Walthall; number of model inversions (locations)=235,680; VIS=visible; NIR=near-infrared channel.

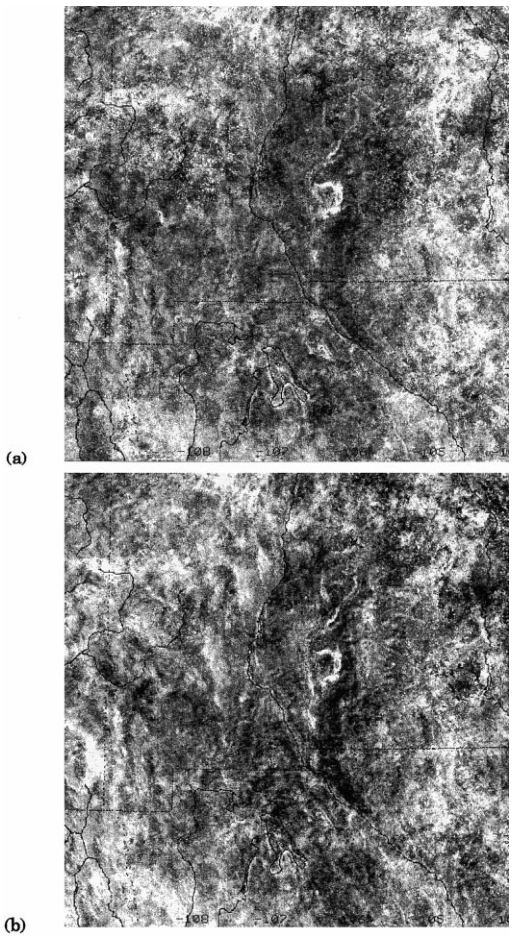

Figure 7. Spatial distribution of RMSE on fitting LiSparse–RossThin model (all overpasses): a) VIS; b) NIR channel. Displayed via 2-standard deviation stretch; see Table 2 for statistics.

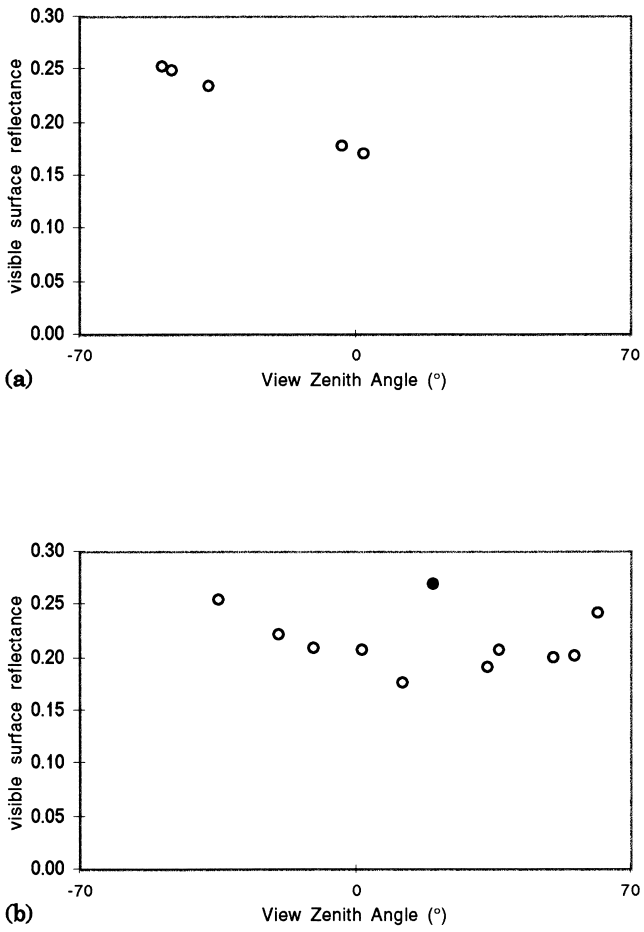

Figure 8. The azimuthal angular sampling series provided by the AVHRRs for the Jornada Experimental Range grassland site (JORNEX grassland site): a) PM overpasses (solar zenith angles are 27–36°) and b) AM overpasses (including evening overpasses; solar zenith angles are 58–78°). The series is screened for cloud and shadow; surface reflectance is estimated using SMAC (see text). Note the typical land BRDF shape, with the exception of the filled datapoint in (b), which corresponds to the evening overpass of NOAA-12 on 28 May at about 7 p.m. (solar zenith angle of 78°).

over land, there has been little discussion of the impact of the shadows cast by clouds on the surface; neither of the two large reprocessing programs designed to provide consistent global AVHRR observations over land, the NOAA/NASA Pathfinder Land and USGS-IGBP 1km AVHRR Land programs, explicitly mention the problem of cloud shadow, although the CLAVR algorithm (Stowe et al., 1991) used to provide cloud masks includes apparent temperature tests which may screen out some shadowed observations. The apparent lack of interest in this problem may be because these programmes are reprocessing only data from the afternoon AVHRRs (on the NOAA-7, -9, -11 and -14 satellites) which have local overpass times which constrain solar zenith angles to be less than 35° and view zenith angles are limited to within 42° of nadir; this means that a good proportion of the shadow cast on the surface by clouds is not visible to the sensor. The higher solar zenith angles for AM overpasses mean that a greater proportion of the shadows cast by clouds are visible to the sensor; however, cloud shadow is still apparent in the PM scenes and cannot be disregarded as an important potential source of contamination. Furthermore, the extent of the problem is dependent on factors other than solar zenith angle, including view zenith, cloud optical thickness, and height above the surface. Recently, more attention has been given to this problem (Simpson and Stitt, 1998).

The challenge for this study was to find a rapid means of detecting anomalous, cloud- and shadow-contaminated observations so that only sets of directly-illuminated clear-to-surface observations are presented to the BRDF model. This could have been achieved by creating separate binary raster image masks based on a variety of tests (e.g., the CLAVR algorithm) to flag contamination, but this has the dual disadvantages of requiring additional disk storage and inflexibility. Instead, an approach was adopted based on temporal consistency in observations in the visible channel over the series of 22 overpasses. This approach has some-

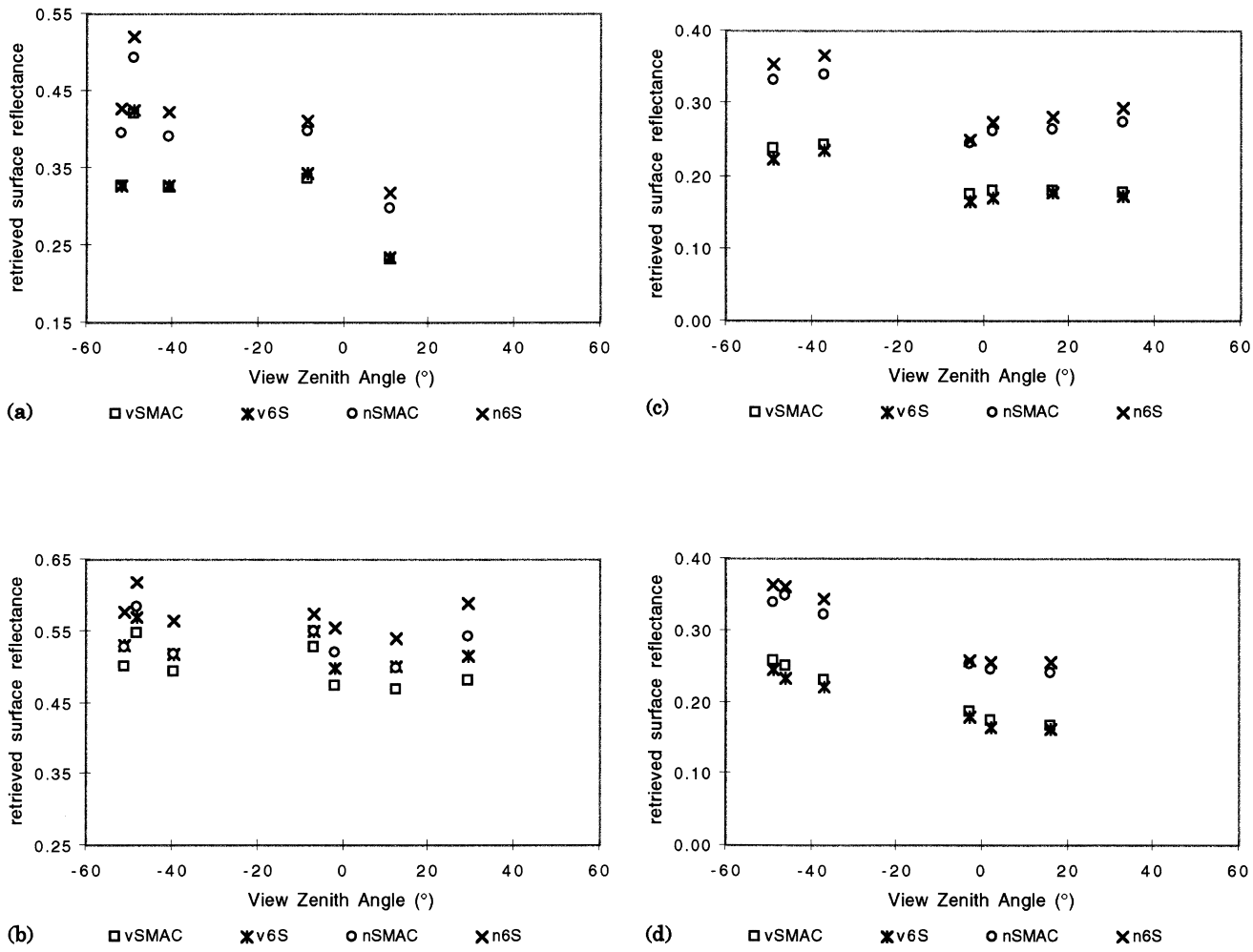

Figure 9. Azimuthal plots of AVHRR surface reflectance retrievals from SMAC and 6Sv4.2 (v=visible, n=near-infrared) for solar zeniths in the range 22–37° (NOAA-14 PM overpasses). Various azimuths not far from the principal plane (see Fig. 1). Sites: a) White Sands gypsum dunes; b) White Sands alkali flats; c) Jornada mesquite dunes; d) Jornada transition; e) Jornada grassland; f) West Tularosa Basin shrubland; g) Sevilleta creosote West; (h) Sevilleta grassland East; (i) Sevilleta creosote East.

thing in common with the cloud shadow algorithm used in the processing of the global LASUR GVI dataset at CESBIO (Centre d'Etudes Spatiales de la Biosphère), Toulouse, France (Berthelot et al., 1997), although these workers used annual maps of minimum visible channel reflectance based on the date of maximum NDVI. The assumptions on which the screening implemented here is based is that the main sources of variation in a series of observations over the same point and over a 33-day period are limited to the following, listed in likely order of magnitude:

- cloud contamination,
- cloud shadow contamination,
- changing from dry to wet soil following rainfall,
- changes in vegetation status owing to fire,
- BRDF effects,
- changes in atmospheric path length (a function of quality of atmospheric correction),
- changes in atmospheric composition (water vapour, ozone, aerosols, volcanic plumes),
- changes in vegetation status owing to growth, senescence, and grazing,
- errors in registration (navigation),
- changes in the area and shape of the projection of the sensor's instantaneous field-of-view on the ground with scan angle (Baldwin and Emery, 1998; Privette et al., 1996; Goward et al., 1991).

Note that changes in soil reflectance owing to rainfall do not impact severely on the AVHRR data used in this study over the Jornada JER and Sevilleta NWR sites (see the first subsection of this section), although no explicit information on the spatial distribution of precipitation is available over the entire area and arid and semiarid regions exhibit a notoriously high degree of variability in both spatial and temporal distributions of precipitation. An important assumption is that the number of clear-to-surface observations is likely to be much greater than the number of contaminated samples over the period and this seems reasonable (i.e., it is usually sunny in southern New Mexico

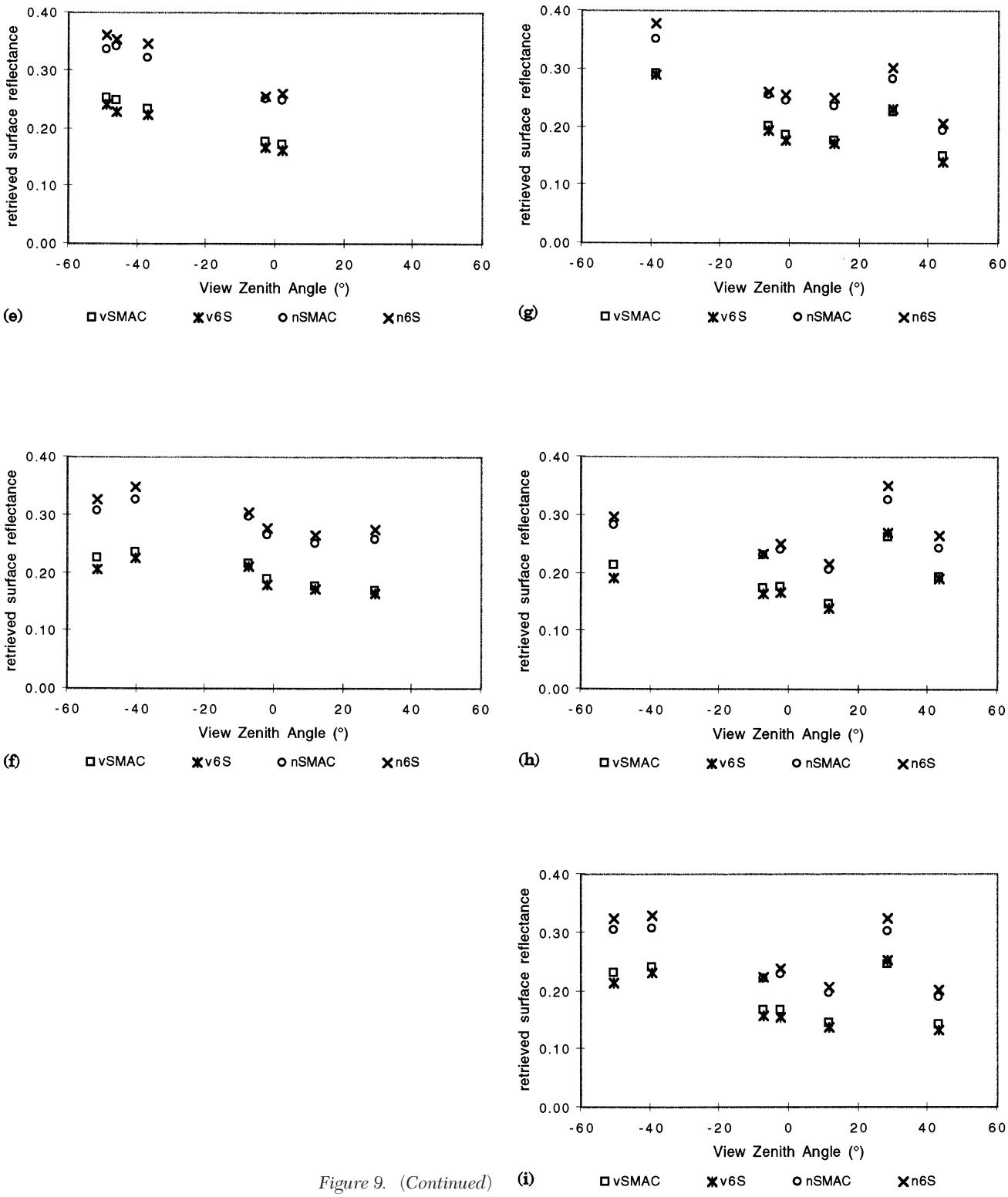

Figure 9. (Continued)

at this time of year). The major disadvantage of this approach is that cloud shadow falling on a very dark surface and/or thin cloud over a very bright land surface may not be screened out; however, in these instances the impact is less important. Important advantages are that anomalous values resulting from data dropouts or other errors are removed and will not be forwarded to the inversion algorithm and that observations suddenly darkened as a result of soil wetting are also likely to be screened out (although this has not been demonstrated here).

Rather stringent methods are required to screen out both cloud and cloud shadow and yet retain very bright

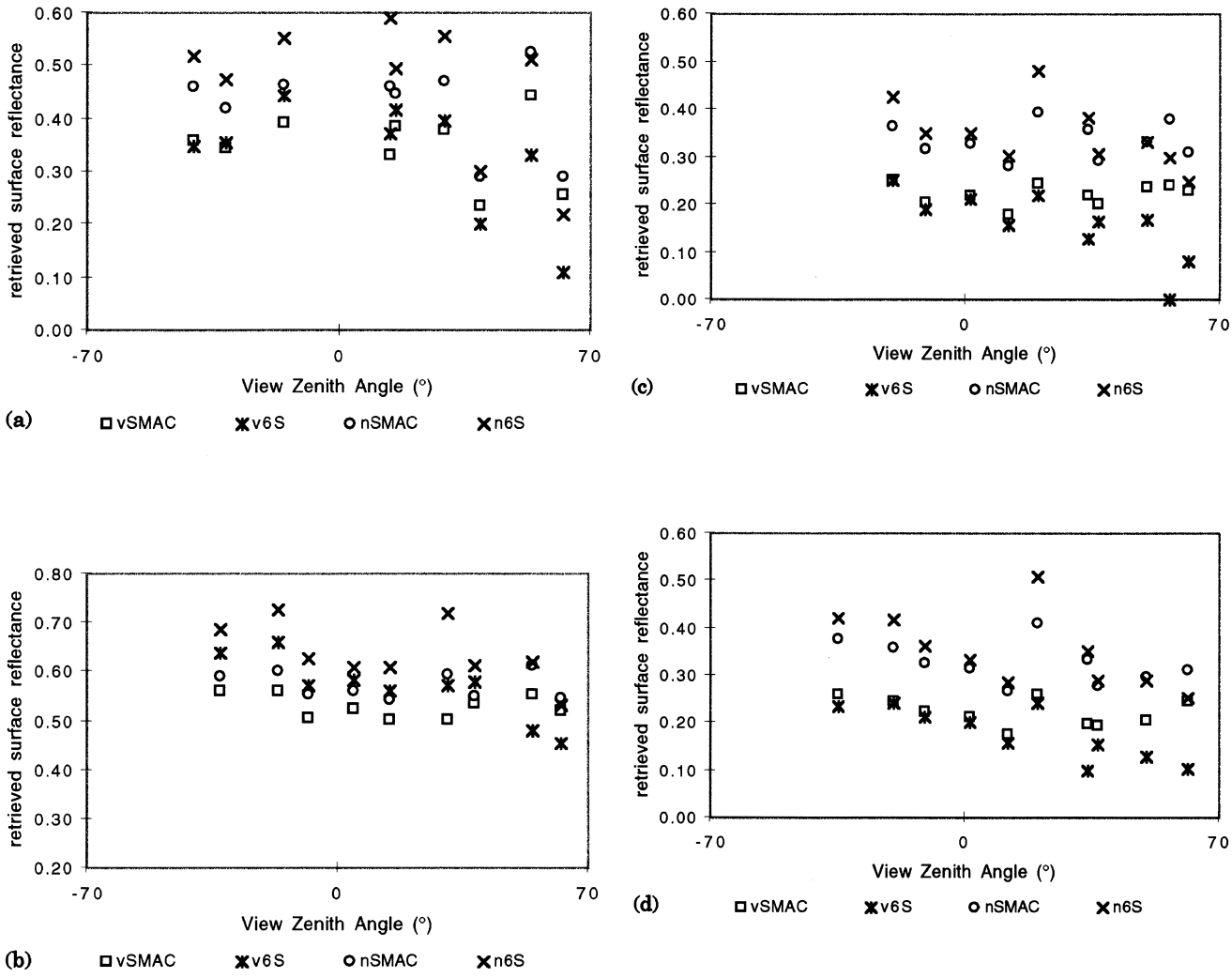

Figure 10. Azimuthal plots of AVHRR surface reflectance retrievals from SMAC and 6Sv4.2 (v=visible, n=near-infrared) for solar zeniths in the range 57–79° (NOAA-12 AM and evening overpasses). Various azimuths not far from the principal plane (see Fig. 1). Sites: a) White Sands gypsum dunes; b) White Sands alkali flats; c) Jornada mesquite dunes; d) Jornada transition; e) Jornada grassland; f) West Tularosa Basin shrubland; g) Sevilleta creosote West; h) Sevilleta grassland East; i) Sevilleta creosote East.

features; fixed thresholds based on a series mean do not work well since the mean is sensitive to outliers, both in number and in magnitude. The most extreme outliers resulting in anomalous series means are from cloud and are a more frequent problem than shadow (since clouds tend to obscure their own shadows); reflectance values can be very high. To arrive at a better measure of average surface reflectance over the series, the criterion of the series means plus 0.8 times the population standard deviation is used to screen out high values from cloud; new means, and standard deviations are then calculated from the reduced series. This variable threshold is used rather than a fixed one such as 0.35 visible reflectance, since the latter would eliminate bright features such as White Sands alkali flats, gypsum dunes, and dry lake beds. Upper and lower thresholds are then set at the new mean ± 1.8 and ± 1.4 population standard deviations, respectively, found by examining the series for about 20 locations with obvious contamination. For the overpasses used here, the technique gives rather good results and has the advantages of simplicity, rapidity, and consistency. Note that the thresholds are set conservatively; that is, to preferentially exclude questionable observations (Figs. 3a–h). Observations deemed to be contaminated or out-of-range are tagged in the reflectance images output by negation: If the input reflectance is less than zero, then zero is output; if the input reflectance is outside the limits, then it is negated before output; and if the input reflectance is within the limits, then it is output with no further modification.

The quality and the limitations of this screening are illustrated by pairs of scene printouts, as in Figures 4 and 5. For the pairs of printouts the first (a) is the unscreened atmospherically-corrected scene, while in the second (b), those observations tagged as contaminated at the screening stage are color-coded and the clear-to-surface observations are shown in greyscale. The unscreened scenes are dis-

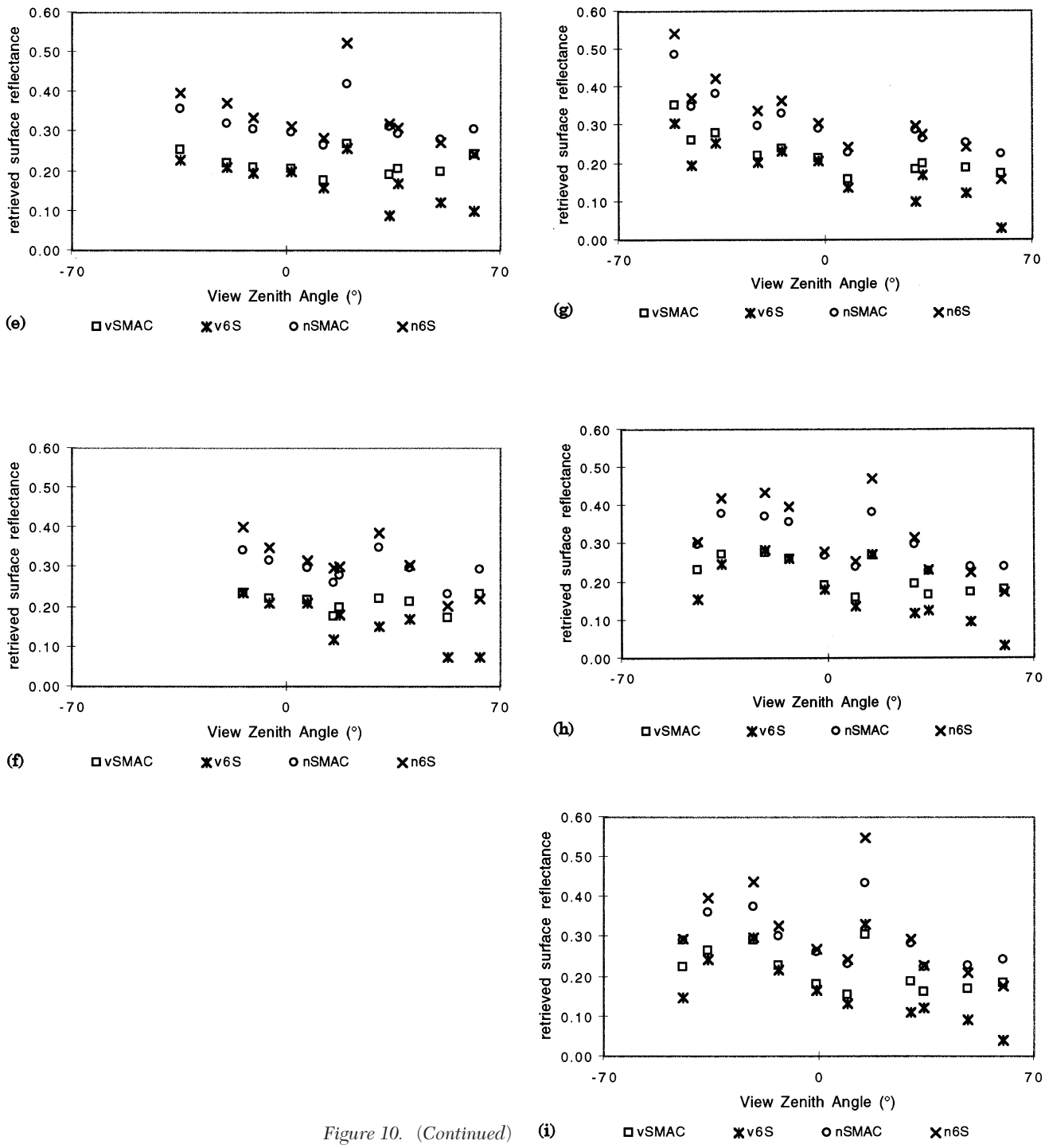

Figure 10. (*Continued*)

played via a linear contrast stretch to 2 standard deviations, while the screened scenes are displayed in pseudocolor via two lookup tables; one color and one greyscale (both tables in equal-area scaling). The color coding used for the screened observations, from lower to higher absolute reflectance values, is: violet, indigo, dark blue, light blue, dark green, light green, yellow, orange, red (inverse ROYGBIV scale). For most scenes, those observations screened out as a result of being too low (e.g., cloud shadow) are shown in Figures 4 and 5 in purple and dark blue, while those screened out as a result of being too high (e.g., cloud) are shown in the remaining colors, with very highly-reflective cloud appearing in yellow and red. It is clear that the lower threshold is sometimes unable to distinguish between shadowed observations and those which have a low surface reflectance. Moreover, reflectance from thin and subsample-sized cloud may result in values below the upper threshold and may thus sometimes be retained.

Table 3. Number of Occurrences of Uncertain Surface Reflectance Retrievals per Overpass (Absolute Difference between SMAC and 6Sv4.2 Retrievals>0.05), in Nine Sampled Locations (Those Listed in Table 5 plus White Sands Dunes, White Sands Alkali Flats, and West Tularose Basin Shrubland)

	Number of Occurrences		
Filename[a]	*Both*	*Channel 1*	*Channel 2*
n12_970603_0027	10	6	4
n12_970515_1441	17	9	8
n12_970602_0049	10	8	2
n12_970527_1338	9	1	8
n12_970528_0059	7	1	6

[a] See Table 1 for details.

BRDF Model Inversions

The BRDF models are inverted for the Channel 1 and 2 reflectances separately since the surface-radiation interactions governing the BRDF are wavelength-dependent. For these linear semiempirical models (Roujean et al., 1992b; Wanner et al., 1995; Strahler et al., 1996), one isotropic and two anisotropic kernels are inverted at a time, providing three model parameter images and one RMSE image for each channel. Note that where the Roujean model is referenced, the full Roujean model (Roujean et al., 1992b) is intended rather than the Roujean geometric-optical function. The empirical modified Walthall model is also inverted to provide four parameter images and one RMSE image. Model inversion is accomplished analytically by matrix inversion methods via the AMBRALS code, with one model considered at a time. The semiempirical kernels used are the LiSparseMODIS geometric-optical kernel and the RossThin and RossThick kernels, which are approximations to Ross's radiative transfer theory (Ross, 1981) for optically thin and thick cases, respectively. The LiSparseMODIS kernel is derived from a consideration of light scattering in forestlike canopies which are composed of sparsely spaced discrete crowns, including mutual shadowing of crowns (Li and Strahler, 1992); this model is appropriate since the study area is dominated by shrubland with most of the forested areas characterized by open, sparse canopies. The kernel is formulated with the two internal parameters which define crown shape and height set at the MODIS default values for a spherical crown shape with the height of the crown center above the ground equal to crown diameter; where the LiSparse kernel is referenced the MODIS version is intended. Future research will examine the impact of changing these values to represent the rather low, oblate crown shapes of mesquite, creosote, and tarbush shrublands.

This processing differs from some other schemes in some important respects. For example, adjustment of POLDER observations against the Roujean model (Roujean et al., 1992b) is achieved via a two-stage procedure (Leroy et al., 1996). This involves an initial model inversion on a set of contamination-screened bidirectional reflectance observations and if the distance of an observation from the model is more than twice the overall RMSE in model fitting, the observation is rejected and the regression reapplied on the remaining set. Clearly, this technique will eliminate observations which differ greatly from the bulk directional behavior and will thus lead to lower RMSE values on the final adjustment of the model. The reason for adopting the technique is to screen for instrumental noise, or inaccuracies of cloud detection and atmospheric corrections (Leroy et al., 1996). However, lower RMSE on model fitting is not the only criterion by which the quality of inversion is judged here, and so no secondary screening is carried out. Note that the AMBRALS version 2.4 (beta) code used for BRDF model inversion was corrected for an error in the calculation of relative azimuth angles and adapted to additionally provide the Roujean volume-scattering kernel (Roujean et al., 1992b) and the weight of determination (a measure of expected error in model parameters and modeled reflectance; see Lewis and Wanner 1996) by writing the inverse matrices used to solve the 235,680 inversion problems.

RESULTS

Impact of Screening: Observations Forwarded to the Models

When all overpasses are used, the minimum number of observations forwarded to the BRDF models for a single location is 10 and the maximum is 21, with most locations

Table 4. Statistics for Images of Retrieved Isotropic Model Parameters for the LiSparseMODIS–RossThin and LiSparseMODIS–RossThick Models[a]

Model:	*LSRn*	*LSRk*	*LSRn*	*LSRk*	*LSRn*	*LSRk*	*LSRn*	*LSRk*
# Orbits:	*22*	*22*	*17*	*17*	*22*	*22*	*17*	*17*
Channel:	*VIS*	*VIS*	*VIS*	*VIS*	*NIR*	*NIR*	*NIR*	*NIR*
Minimum	0.02	0.03	−0.03	−0.03	0.07	0.11	−0.03	−0.02
Maximum	0.59	0.58	0.58	0.57	0.62	0.61	0.62	0.62
Mean	0.19	0.18	0.18	0.18	0.25	0.24	0.25	0.24
Median	0.19	0.18	0.18	0.18	0.25	0.24	0.25	0.24
Mode	0.19	0.18	0.19	0.18	0.25	0.24	0.26	0.25
St. dev.	0.05	0.05	0.05	0.05	0.04	0.04	0.04	0.04

Models are isotropic kernel (unity) plus LS=LiSparseMODIS, Rn=RossThin, Rk=RossThick; VIS=visible, NIR=near-infrared channel.

Table 5. Retrieved LiSK Model Parameters over Research Sites at the Jornada and Sevilleta Ranges, RMS Error (Absolute) in Model *Fitting and Leaf Area Index* (LAI)[a]

	Visible Channel					*Near-Infrared Channel*			
Site	*LAI*	*ISO*	*GO*	*VOL*	*RMSE*	*ISO*	*GO*	*VOL*	*RMSE*
Sevilleta creosote (West)	0.220	0.227	0.026	0.029	0.030	0.278	0.022	0.034	0.038
Sevilleta grassland (Deep Well)	0.820	0.187	0.000	0.014	0.042	0.236	−0.009	0.014	0.052
Sevilleta creosote (East:Five Pts)	1.140	0.184	0.005	0.021	0.046	0.232	−0.003	0.022	0.057
Jornada mesquite dunes site	0.950	0.204	0.012	0.025	0.020	0.281	0.006	0.031	0.025
Jornada transition site	0.590	0.209	0.016	0.027	0.024	0.279	0.011	0.035	0.032
Jornada grassland site	0.400	0.210	0.013	0.022	0.027	0.281	0.009	0.028	0.035

[a] ISO=isotropic, GO=geometric-optical and VOL=Volume Scattering. Inversions with isotropic-LiSparseMODIS–RossThin model on all overpasses. LAI measurements were made in late May 1997 over 100 m+ transects.

provided with 16 or 17 multiangular reflectance inputs (Fig. 1b; Fig. 6a). When 17 overpasses are used, the range falls to 7–13 observations with most locations provided with 13 inputs. Assuming that only valid observations are included, the sampling can be deemed adequate in terms of number, with inversion quality more highly dependent on the angular distribution of samples. Sensitivity studies on ground-based multiangular radiometry datasets (Privette et al., 1997; Chopping, 1998c) have shown that parameter retrievals are stable with respect to number of observations above a rather low critical threshold as long as the angular distribution is not too narrow. This is unlikely to be the case since reflectance data are derived from both AM and PM satellites.

Model Fits to Observations

The root-mean-square error on model fitting (RMSE) using data from 22 orbits is generally low and the mode is

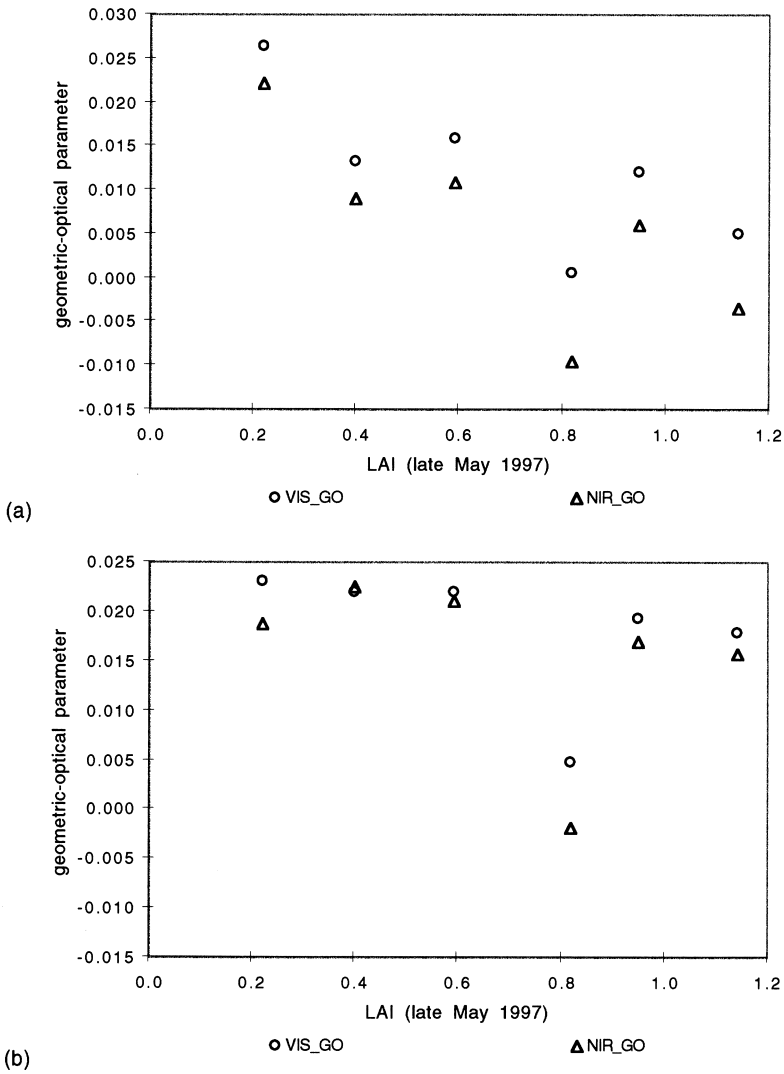

Figure 11. LiSparseMODIS geometric-optical parameter from visible (VIS_GO) and near-infrared (NIR_GO) channel inversions as a function of leaf area index (LAI) for the six sites listed in Table 6: a) models inverted using all 22 overpasses; b) models inverted using only 17 overpasses. LAI measurements made late May 1997 over 100 m + transects.

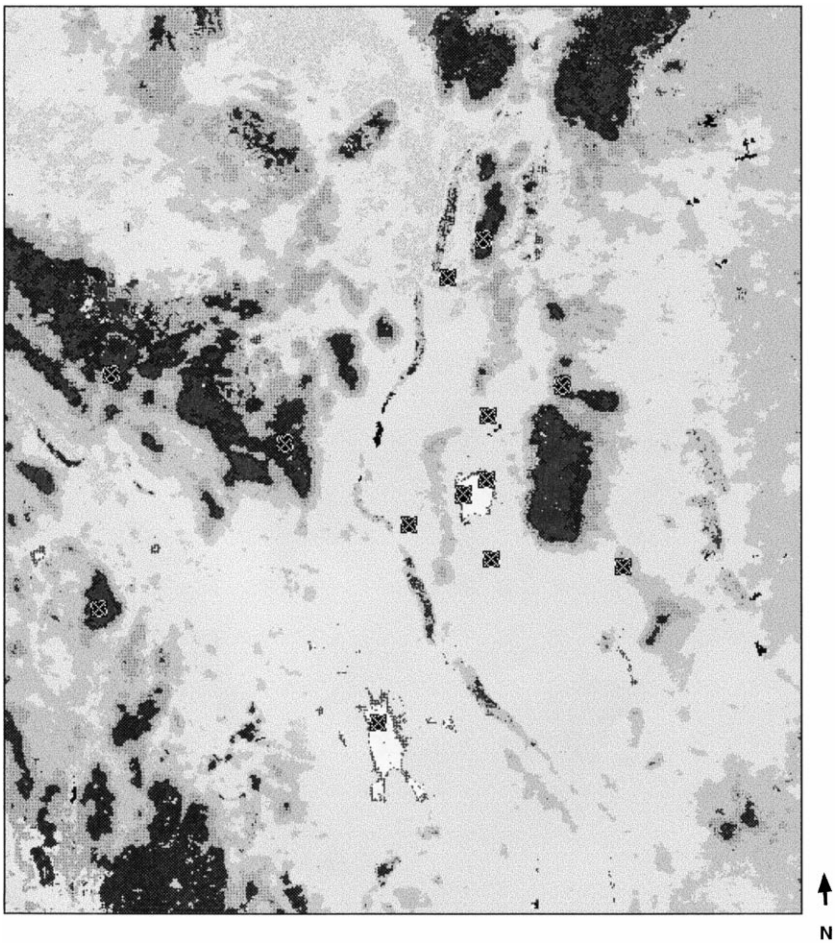

Figure 12. Locations of sites over various land covers (crosses). In order of decreasing latitude : Cibola National Forest (Isleta), Sevilleta Grassland, Apache National Forest, Lincoln National Forest (northernmost-dense), lava flow north of White Sands flats, Black Range (Gila National Forest), White Sands gypsum dunes, White Sands alkali flats, mesquite shrubland (JER), West Tularosa Basin shrubland, Lincoln National Forest (southernmost-sparse), Coronado National Forest (Arizona), and dry lakebed West of Lucero (Mexico). White: barren, very light gray: desert shrubland/grassland, light gray: mixed grassland/shrubland, medium gray: pinyon juniper woodland, dark gray: evergreen needleleaf forest, very dark gray: open needleleaf forest. Source: based on the North America Land Cover Characteristics data base (Loveland et al., 1991).

in the range 0.027 to 0.036, with slightly better fits in the visible channel and little difference between the models (Table 2). Large RMSE values (e.g., >0.07 reflectance) account for 0.05% and 1.20% for the Channel 1 and 2 LiSparse–RossThin inversions, respectively; and 0.62% and 1.67% for the Channel 1 and 2 LiSparse–RossThick inversions, respectively. The spatial distribution of error values is similar for both models and exhibits some structure and several features are apparent in both the visible or near-infrared RMSE images. These include the area corresponding to the dunes of White Sands National Monument which surround the White Sands alkali flats (Fig. 7); poorer model fits are also found for parts of the Gila National Forest in the west; the lava flow just north of White Sands National Monument; the Coronado National Forest in the extreme southwest of New Mexico; in scattered locations in the eastern part of the state; and around the edges of the large dry lake bed to the west of the town of Lucero in Chihuahua, northern Mexico.

With such a large number of inversions, it is impractical to examine residuals from model fitting for every location and orbit. In order to check that there are no gross errors in processing the reflectance or Sun–sensor geometry, residuals were calculated for a small number of locations across the study area. It is apparent from these that data from one overpass in particular (the evening overpass of NOAA-12 on 28 May) impinges on model inversions; that is, these data are contributing disproportionately to total RMS error. In order to determine the nature of the anomaly, reflectance data extracted for selected locations were partitioned by solar zenith angle into two sets and plotted against view zenith angle. These plots show that the reflectance values from the overpass in question fall in the forward scattering direction and are much higher than would be expected; these data do not fit the characteristic bowl shape of the land BRDF (Fig. 8). On inspection of the visible channel imagery it is clear that this scene is subject to much thin cloud which is difficult to detect but—more importantly—solar zenith angles are very high (>78°), presenting problems for the atmospheric correction algorithm and resulting in very low land reflectance values. Note that SMAC is based on 5S and versions of 5S/6S prior to 6Sv4.1 are not well-adapted to extreme angles.

In order to check that the surface reflectances retrieved via the SMAC algorithm are reasonable, the Channel 1 and 2 spectral radiances for the sites listed in Table 5 plus three others (White Sands gypsum dunes, White Sands alkali flats, and W. Tularosa Basin shrubland) were

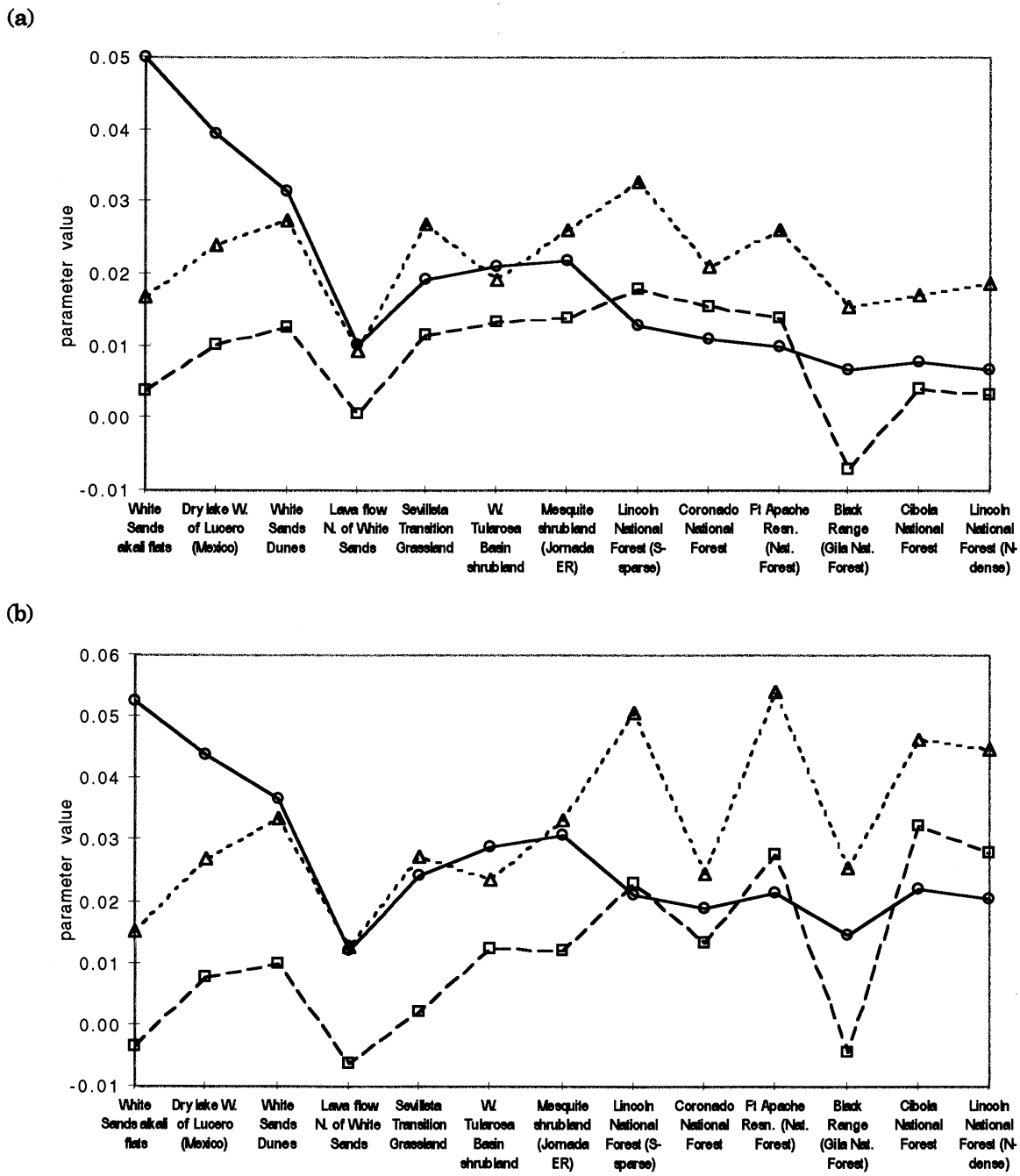

Figure 13. Isotropic-LiSparseMODIS–RossThin parameters for a range of land cover types, in NDVI order: c) Channel 1 and d) Channel 2 inversions, 17 overpasses. Circles are isotropic parameter values × 0.1; squares and triangles are geometric-optical and volume scattering parameters, respectively. Lines are for clarity of reading only.

submitted to 6S version 4.2 (no geometric restrictions, midlatitude summer atmosphere model, continental aerosols model, 20 km visibility). The retrieved surface reflectance estimates are reasonably similar for all afternoon satellite overpasses (low solar zeniths; Fig. 9) but differ in some instances in morning and evening overpasses (high solar zeniths; Fig. 10). Five overpasses in particular appear to cause difficulties for stable surface reflectance retrievals, with SMAC and 6S v4.2 underestimating and overestimating the impact of high solar zeniths, respectively. On counting the number of times each overpass results in divergences of more than 0.05 (reflectance) between the codes, it is clear that all three NOAA-12 evening overpasses and two other NOAA-12 morning overpasses present problems (Table 3).

In view of the problems in determining surface reflectance accurately from these five overpasses, the models were inverted again using a reduced set of 17 overpasses.

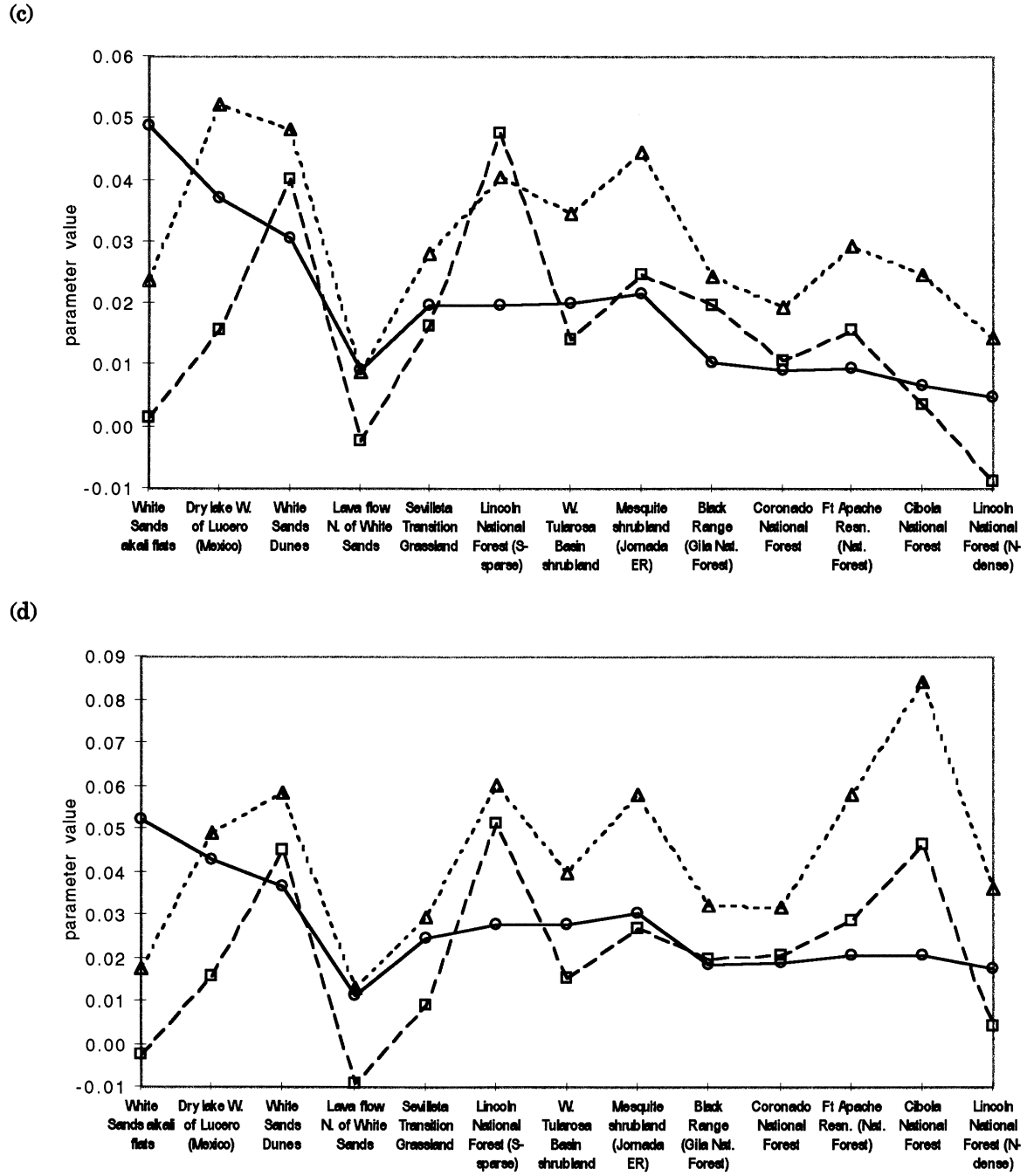

Figure 13. (*Continued*)

The reduced set provides a smaller number of angular observations (7–16 instead of 10–12; see Fig. 6b) but also lower RMSE values in inversions on both visible and near-infrared reflectances, with modes (previous values) of 0.019 (0.027) and 0.026 (0.033), respectively, for the isotropic-LiSparseMODIS-RossThin model and 0.019 (0.026) and 0.025 (0.036) for the isotropic-LiSparseMODIS-RossThick model (Table 2). When only 17 overpasses are used, large RMSE values (e.g., >0.07 reflectance) account for 1.76% and 1.78% for the Channel 1 and 2 LiSparse–RossThin inversions, respectively, and 1.61% and 1.49% for the Channel 1 and 2 LiSparse–RossThick inversions, respectively.

Retrieved Model Parameters

The models are formulated so that the isotropic parameter represents nadir reflectance with the overhead sun (Roujean et al., 1992b). The values retrieved (using all overpasses) are always reasonable and lie in the range 0.02–0.62 over both channels for both the LiSparse–Ross models, with means of ~0.18 and ~0.25 and standard

Table 6. Statistics for Images of Weights of Determination Values for Model Parameters Using All 22 Orbits and a Reduced Set of 17 Orbits[a]

Model:	*Ln*	*Lk*	*Rou*	*Ln*	*Lk*	*Rou*	*Ln*	*Lk*	*Rou*	*Ln*	*Lk*	*Rou*	*Ln*	*Lk*	*Rou*
# Orbits:	22	22	22	17	17	17	22	22	22	17	17	17	22	22	22	17	17	17
Params:	*ISO*	*ISO*	*ISO*	*ISO*	*ISO*	*ISO*	*GO*	*GO*	*GO*	*GO*	*GO*	*GO*	*VOL*	*VOL*	*VOL*	*VOL*	*VOL*	*VOL*
Min	0.2	0.2	0.2	0.2	0.2	0.2	0.0	0.0	0.0	0.1	0.0	0.0	0.0	0.5	**1.9**	0.0	0.7	**3.6**
Max	**1.6**	**1.6**	0.7	**14.6**	**6.5**	**6.5**	0.2	0.2	0.4	**8.5**	**1.0**	**1.0**	**11.2**	**10.6**	**61.3**	**11.2**	**114.8**	**637.5**
Mean	0.3	0.3	0.2	0.3	0.3	0.3	0.0	0.0	0.1	0.1	0.1	0.1	0.1	**2.2**	**11.4**	0.1	**3.6**	**19.9**
Median	0.3	0.2	0.2	0.3	0.3	0.3	0.0	0.0	0.1	0.1	0.1	0.1	0.1	**2.2**	**10.7**	0.1	**2.4**	**13.5**
Mode	0.3	0.2	0.2	0.3	0.3	0.3	0.0	0.0	0.1	0.1	0.1	0.1	0.1	**2.4**	**7.7**	0.1	**1.5**	**8.6**
St. Dev.	0.1	0.1	0.0	0.1	0.1	0.1	0.0	0.0	0.0	0.1	0.0	0.0	0.1	0.8	**5.2**	0.1	**2.4**	**13.5**

[a] ISO=isotropic, GO=geometric-optical and VOL=volume scattering. Kernels: iso= isotropic (unity), L=LiSparseMODIS, n=RossThin, k=RossThick, Rou=Roujean GORT model.

deviations of ~0.05 and ~0.04 for the visible and near-infrared wavelengths, respectively (Table 4). There is little difference in distributions when only 17 overpasses are used. The proportion of negative anisotropic parameter values for the isotropic-LiSparse–RossThin inversions is rather low (i.e., around 2.5% and 3.7% for the visible channel geometric-optical and volume scattering parameters, respectively, and 5.7% and 5.0% for the near-infrared channel geometric-optical and volume scattering parameters, respectively), and such values are usually apparent over surface types for which the model is not well adapted, for example, over parts of the Gila National Forest in the west (and particularly deciduous broadleaf forest), White Sands alkali flats and dunes, lava flows, and parts of the densely-forested Mescalero Apache Indian reservation to the east of White Sands. For the LiSparse–RossThick model, the proportion of retrieved parameters which are negative is much larger: 30.6% and 62.5% for the visible and near-infrared geometric-optical parameters, respectively, and 4.0% and 9.9% for the visible and near-infrared volume scattering parameters, respectively. Similarly, the Roujean model provides 22.3% and 43.1% and 0.3% and 0.6% negative values for the same channels and parameters, respectively.

Negative parameter values are retrieved when better fits to observations are obtained if one of the kernels is inverted (i.e., it is used "upside-down"); in this situation no physical interpretation of parameters is possible. Negative parameter values are therefore undesirable. It is unusual for both anisotropic parameters to be negative, and this situation is only rarely encountered; it is also more usual for the geometric-optical kernel to be inverted than the volume scattering kernel. Note that negative parameters occur in locations where the parameter values trend toward a local minimum; they do not tend to occur as isolated points. Note too that there is a spatial correspondence between negative parameters retrieved for visible and near-infrared model inversions, although negative values are more often associated with near-infrared inversions, probably as a result of a more important multiple scattering component which is not accounted for in the models (the contribution is assumed isotropic).

Since both the Jornada Experimental Range and the Sevilleta National Wildlife Refuge are within the study area, it is possible to compare retrieved parameters against sites with known characteristics (Table 5). The visible channel geometric-optical parameters show a palpable relationship to leaf area index (LAI) values measured with a LiCor 2000 between 25 and 31 May 1997 at six sites in the Sevilleta and Jornada rangelands (Fig. 11). Similar relationships are found for a clumping index composed by normalizing the geometric-optical parameter to the isotropic parameter (Lacaze and Roujean, 1997). While it is difficult to argue that there should be an intrinsic linear relationship between leaf area and geometric phenomena, since the degree of shadowing will depend on the gap probability

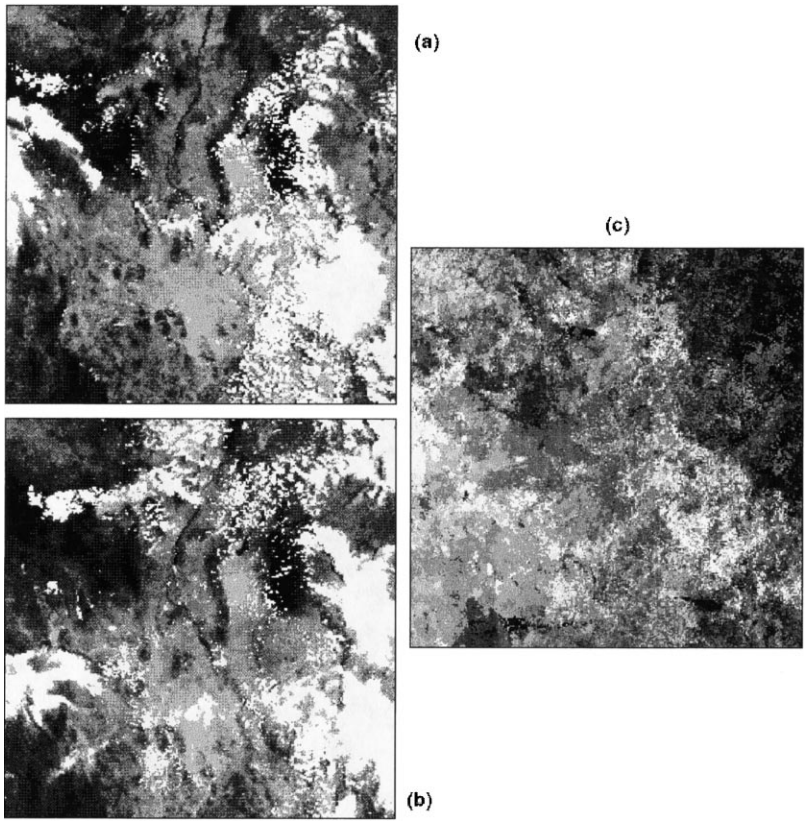

Figure 14. Impact of clouds on noise inflation as a result of restricted angular sampling: a) visible channel reflectance from NOAA-14 AVHRR, 28 May 21:29 GMT; b) *ditto* for 29 May 21:18 GMT; c) weight of determination image for GO parameter (isotropic-LiSparseMODIS–RossThin model). Cloud and shadow both shown in white in reflectance images; other values in shades of gray.

of the canopy as well as the size and shape of shadowing elements (here mostly shrubs but also some cactii, forbs, and grass clumps), the implication is that shadowing is less important in the grassland sites than in the shrub-dominated sites and this explanation is plausible. If only 17 overpasses are used in model inversions, the result is fairly similar for the shrub-dominated sites, although the Sevilleta grassland site on the eastern side of the Rio Grande (known as "Five Points") demonstrates a much lower GO parameter value. Again, this is consistent with the expectation of lower shadowing effects in a more homogeneous grassland with only sparse shrubs and cactii. Note that in both cases the behavior with LAI is similar for inversions on both visible and near-infrared reflectance data, providing further evidence that this parameter is related to the structural rather than the spectral characteristics of the canopy-soil complex.

The rapid inversion of BRDF models over such an extensive area allows examination of retrieved parameter values for widely-differing land cover types. Sites were selected with reference to the AVHRR channel and NDVI imagery and the North America Land Cover Characteristics database (Loveland et al., 1991; Fig. 12). Parameter values for the isotropic-LiSparseMODIS–RossThin BRDF model inversions (using all overpasses) were extracted for these 13 point sites and are plotted in Figures 13a and 13b. RMS errors in model fitting are below 0.05 in every case except the White Sands gypsum dunes; this is hardly surprising, since these dunes exhibit extraordinary reflectance properties in both magnitude (brightness) and directionality (almost Lambertian). All weight of determination values for the parameters are below unity, indicating negligible noise inflation. The retrieved anisotropic parameters are largely uncorrelated with the isotropic parameter, with $r^2<0.03$ and <0.07 for the visible and near-infrared inversions, respectively. In both the visible and near-infrared inversions the behavior with cover type is similar, although the anisotropic parameters are highly correlated (coefficient of determination is 0.63 for the visible parameters and 0.79 for the near-infrared parameters). It is probable that this high degree of correlation is owing to the sparseness of canopies in this region at this time of the year when grasses are dormant: Where shrubs and trees are more leafy (increasing volume scattering), shadowing also becomes more important (shadows are larger and darker). In a previous study over the semiarid grasslands of Xilingol, Inner Mongolia centered on eight sites and using data from 21 AVHRR overpasses (Chopping 1998a,b,c), correlation between the anisotropic parameters was very low for both channels with $r^2<0.04$. However, the Inner Mongolia study was carried out over grasslands with far smaller shrub : grass ratios and at the peak of the growing season (August 1996) when the grasses are green, cover higher, and the canopies less discontinuous. The discrepancy may be an indication of problems with the calibration for the NOAA-12 AVHRR used in the current study, since 12 of the 22 overpasses were from the AM satellite AVHRR, against 4 out of 21 in the Inner Mongolia study. Other differences

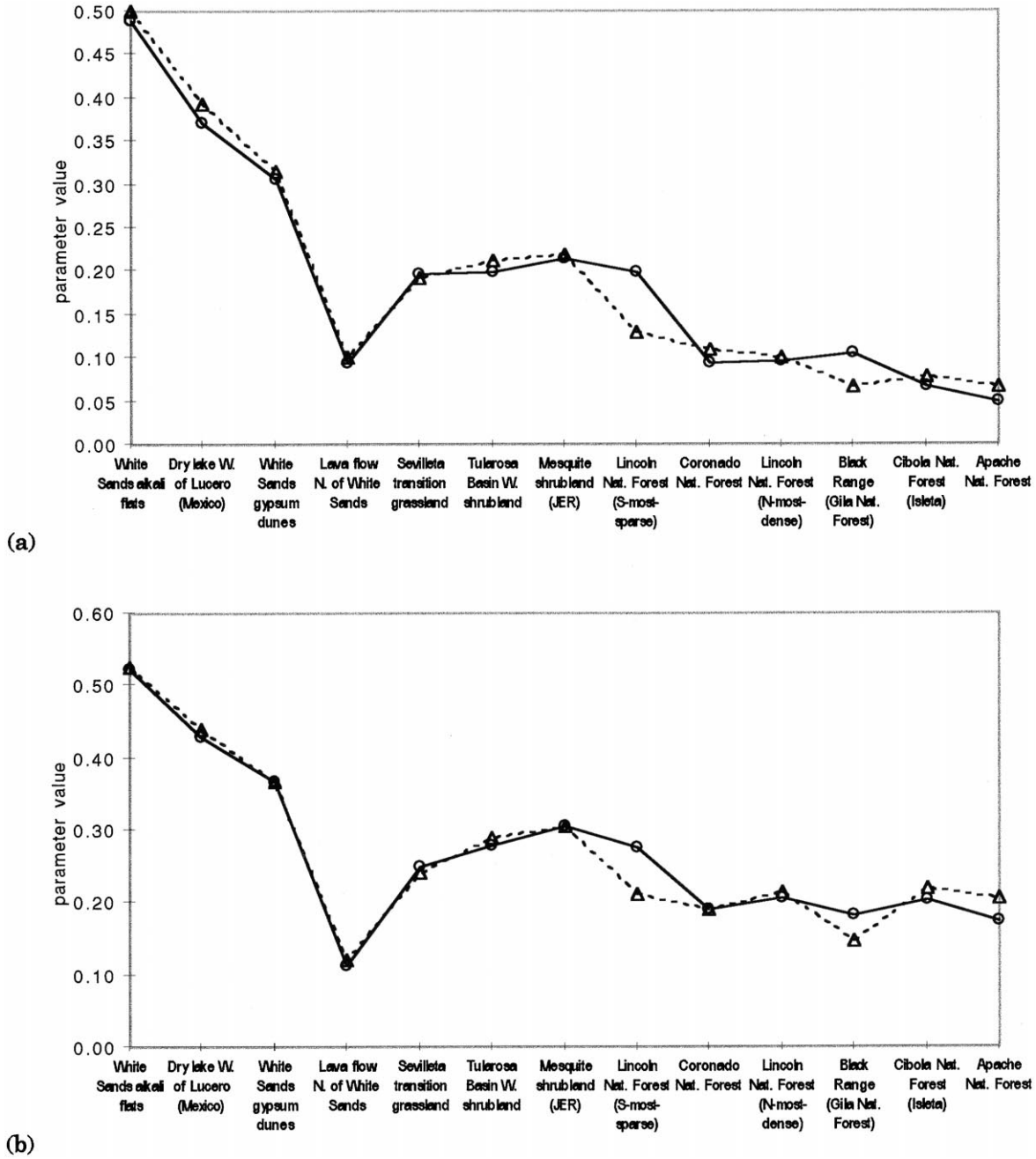

Figure 15. Comparison of retrieved model parameters (Isotropic-LiSparseMODIS–RossThin model) using all 22 AVHRR overpasses (triangles) and just 17 AVHRR overpasses (circles): a) visible isotropic; b) near-infrared isotropic; c) visible geometric-optical; d) near-infrared geometric-optical; e) visible volume scattering; f) near-infrared volume scattering. In NDVI (isotropic) order. Lines joined for clarity of reading only.

are the relatively long data accumulation period (33 days against 17) and the use of site-specific atmospheric parameters for corrections over the entire area.

Parameter values for the isotropic-LiSparseMODIS-RossThin model inversions for the same sites but using the reduced set of 17 overpasses are plotted in Figures 13c and 13d. There is a lower correlation between the visible wavelength anisotropic parameters than before although correlation between the isotropic and anisotropic parameters is increased and a maximum r^2 of 0.29 is found between the visible channel isotropic and volume scattering parameters. Correlation between the near-infrared isotropic and anisotropic parameters is negligible ($r^2<0.0004$ in both cases), although correlation between the anisotropic parameters remains high ($r^2=0.78$).

Impact of Restricted Angular Sampling

The weight of determination images for the model parameters show that where these AVHRR data are used in model calibration, there are less serious noise amplification prob-

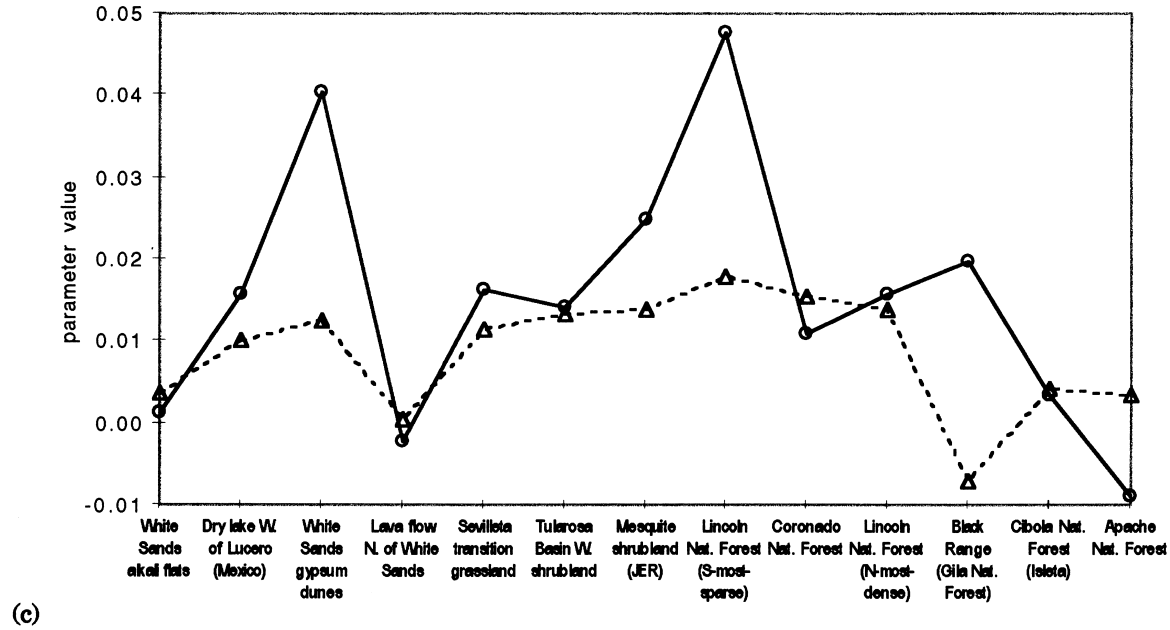

(c)

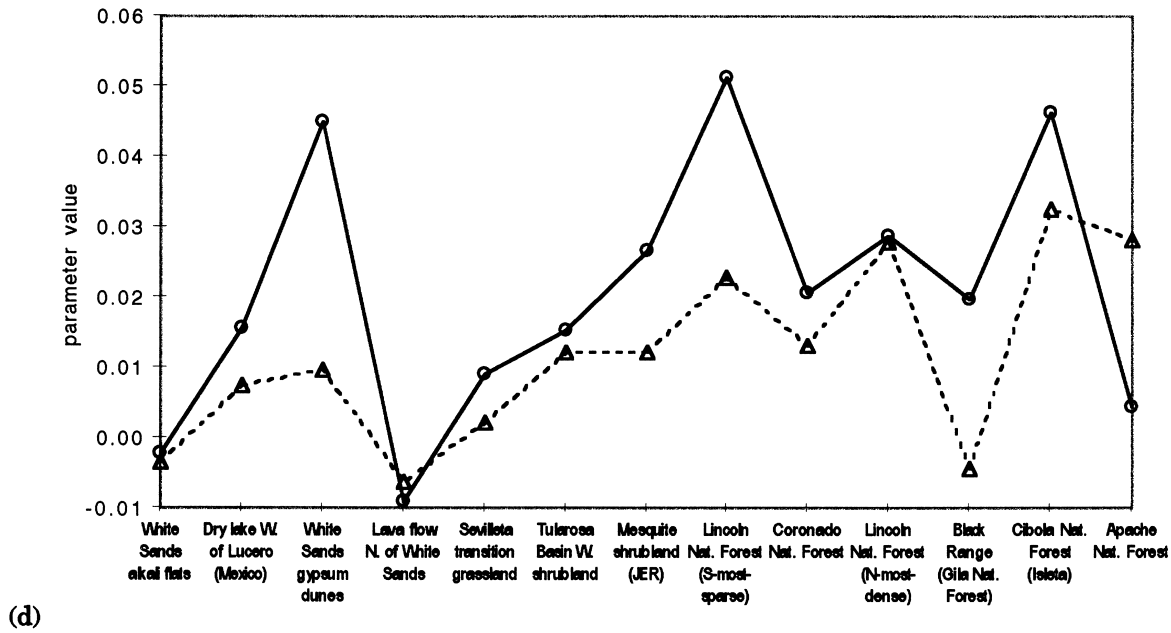

(d)

Figure 15. (*Continued*)

lems in model parameters for the isotropic-LiSparse–RossThin model than for the isotropic-LiSparse–RossThick and 3-kernel Roujean models. In particular, >95% and 100% of weight of determination values for the isotropic-LiSparse–RossThick and Roujean f2 kernel volume scattering parameters are greater than unity, respectively, whether 17 or 22 orbits were used, indicating important noise amplification (Table 6). This compares with 0.7% and 0.0% (zero) for the same parameter for the isotropic-LiSparse–RossThin model. Noise as a result of restricted angular sampling is often a more serious problem for estimating the volume scattering parameter than either the isotropic or geometric-optical parameters (Leroy and Roujean, 1994; Chopping, 1998b), although here noise is lowest for the latter; this may be owing to the large number of AM scenes available. Only the Roujean model exhibited no weights greater than unity in the isotropic parameter.

The structure of the weight of determination image (Fig. 14c) shows that higher values are a result of screening out of observations at some Sun–sensor geometries which would otherwise have contributed disproportionately to an improved angular sampling. This is almost always a result

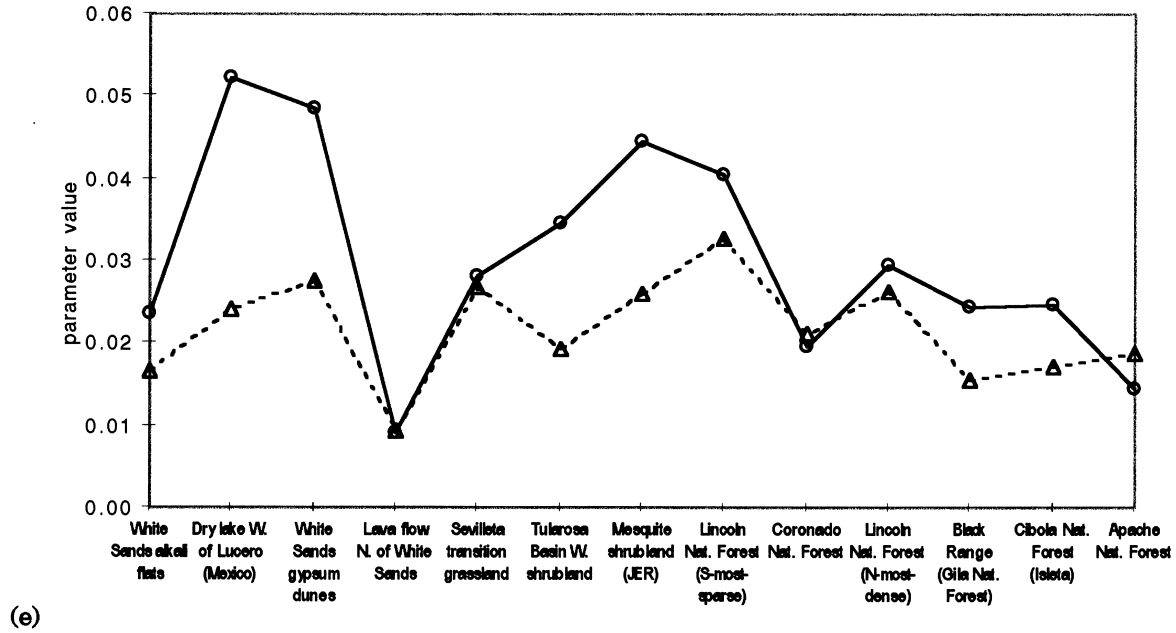

(e)

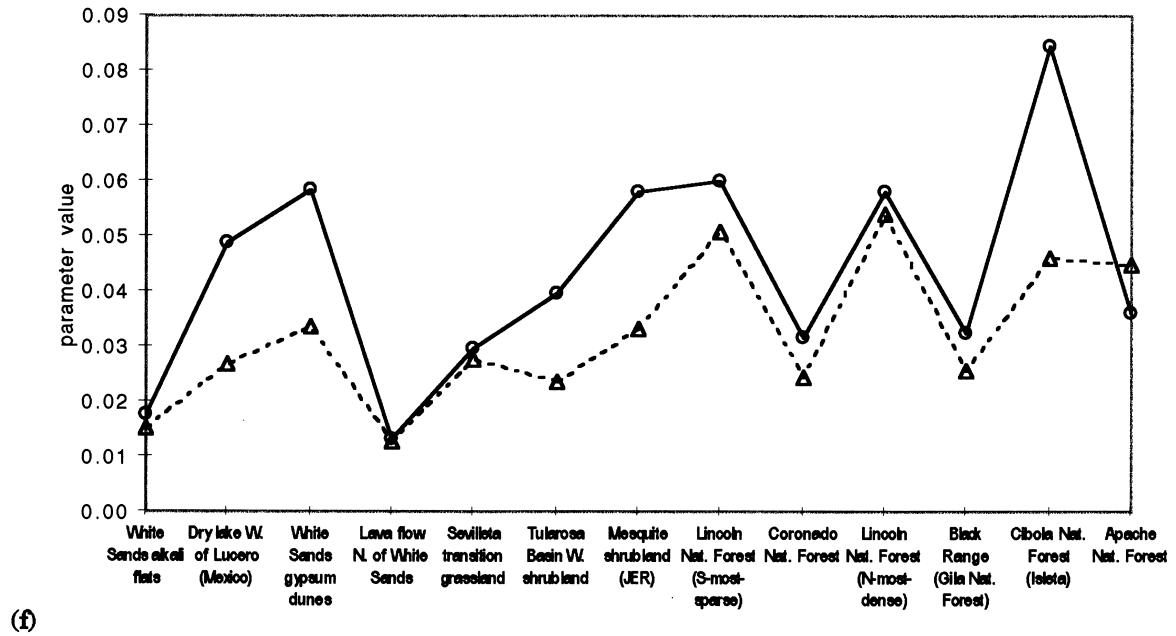

(f)

Figure 15. (*Continued*)

of cloud or cloud-shadowing of the land surface, which reduces the number and range of angular samples. Maximum weight of determination values for model parameters are higher when the isotropic-LiSparse–RossThin model is inverted using the reduced set of 17 overpasses, as would be expected with a more restricted angular sampling, although the distributions are not very different overall, with a very small proportion of values exceeding unity. A similar result is obtained for the isotropic-LiSparseMODIS–RossThick and three-kernel Roujean models, with almost all weight of determination values for the volume scattering parameter image exceeding unity when either 22 or 17 orbits are used in inversion.

The impact of reducing the angular sampling—by removing the overpasses which provide either high solar zeniths or uncertain surface reflectance retrievals—is shown in Figure 15 for the sites shown in Figures 12 and 13. Differences in isotropic parameter values are rather small; however, differences in anisotropic parameters are more important, with the magnitude of differences in the isotropic parameter for vegetated locations matched by larger differences the anisotropic parameters, for example,

for Lincoln National Forest (South-sparse), Black Range (Gila National Forest), and Apache National Forest. Where there is a large difference in one channel, this is generally reflected in another channel; however, a large difference in one anisotropic parameter is not always reflected in the other. Large discrepancies are seen for the White Sands gypsum dunes and the dry lake bed in N. Chihuahua, although these are perhaps not surprising in view of the extreme brightness of the surface at these locations. In general, smaller differences are seen in the volume scattering parameter for darker and more densely vegetated sites.

While noise inflation does not appear to present a problem for inversions of the isotropic-LiSparseMODIS–RossThin model, it is clear that the angular sampling provided by the AVHRRs rarely coincides with a hot spot geometry (Fig. 1). This limits the ability to extract directly information on physical parameters such as leaf size, leaf shape, and leaf angle distribution from multiangular AVHRR data; however, as seen above, it is still possible to gain structural (in addition to spectral) information from these observations.

CONCLUSIONS

As far as is known, this is the first attempt to retrieve BRDF from full resolution AVHRR over an extensive region in central and southern New Mexico and parts of Chihuahua, Mexico. The results show that, in spite of inherent difficulties, such endeavors are very rewarding. In particular, there is usable structural information available from the anisotropic parameters which is not available in the spectral domain (model inversions result in low RMS errors and a low correlation between the isotropic and anisotropic parameters), although this information may not be interpreted directly in terms of physical quantities and there may be problems of noise inflation unless an appropriate model is chosen. In the case of semiarid grasslands and shrublands an isotropic-LiSparseMODIS–RossThin kernel combination appears to be optimal (low RMSE, low proportion of negative retrieved parameters, and low noise inflation in retrieved parameters). Note that although the angular variations in reflectance are described well by the models, BRDF is not necessarily explained; that is, the parameters may not be related to the directional phenomena exactly as intended in the kernel derivations. This may be partly owing to problems with deriving surface reflectances from AVHRR with adequate accuracy; it has been seen that, with solar zenith angles approaching 80°, it is very difficult to obtain reliable surface reflectance estimates. In spite of this, model fits to observations are good for the vast majority of locations, allowing correction of observed values to an optimal chosen Sun–sensor geometry. BRDF correction is in itself an important application which ensures that visible and near-infrared reflectance datasets from the AVHRR are consistent between overpasses, across the seasons, and along the scanline.

It is expected that improvements in retrievals will be possible in the future with revised calibration for the NOAA-12 AVHRR visible and near-infrared channels and more effective contamination screening; it may also be possible to improve surface reflectance retrievals with the greater availability of measured atmospheric parameters (Holben et al., 1998) and codes better adapted to high solar zenith angles. Furthermore, surface BRDF retrieval and surface reflectance retrieval ("atmospheric correction") can be coupled in a converging iteration loop; this has been shown to improve the quality of both retrievals to obtain mean relative errors of less than 1% in surface reflectances even for atmospheric optical depths at 550nm of 0.4 (Hu et al., 1999). There is still the possibility that simplifying assumptions made in the model derivations mean that even if adjusted against a perfectly calibrated multiangular surface reflectance, a physical interpretation of the kernel weights would not be feasible; for example, the assumption of equally bright sunlit ground and sunlit crown in the Li kernels does not seem appropriate in the visible region, where even vegetation adapted to arid conditions is much darker than the soil. Future validation efforts clearly need to be directed to this area. For mesquite and creosote shrublands such as those of the Jornada Experimental Range this will require airborne multiangular acquisitions if a representative sample of features contributing to the surface BRDF is to be included, since a minimum 8–16 m ground-projected field-of-view would be required (Pelgrum et al., 1999). New 3-D scene modeling tools using ray tracing and radiosity techniques will allow the operation of the simplified operational models to be examined from a detailed, theoretical perspective (Lewis, 1996; Qin and Gerstl, 2000).

Large-scale BRDF retrieval via inversions of these LiSK models with data from the two AVHRRs provides an important test of the viability of future regional and global operational retrievals with the MODerate resolution Imaging Spectro-radiometer (MODIS) and Multi-angle Imaging SpectroRadiometer (MISR) sensors on NASA's Terra satellite, while characterizing the directional reflectance behavior of a wide range of southwestern semiarid and arid surface types from spaceborne measurements and allowing corrections for BRDF artifacts in multiangular optical remote sensing data.

Thanks are extended to Jeffrey L. Privette (NASA-GSFC), Daniel Baldwin (University of Colorado), Andrew Hyman (lately of Boston University); Kurt Thome (University of Arizona); Wenge Ni (Raytheon STX); Eric Vermote (NASA-GSFC; 6S); Gérard Dedieu (LOA-Lille; SMAC); Wolfgang Lucht (lately of Boston University, now of Potsdam Institute for Climate Impact Research; AMBRALS); Jerry Ritchie and Al Rango (USDA-ARS Hydrology Laboratory; LAI measurements). I am very grateful to the anonymous reviewers for providing invaluable insights and highlighting errors and omissions in early drafts of the paper.

REFERENCES

Asner, G. P., Braswell, B. H., Schimel, D. S., and Wessman, C. A. (1998), Ecological research needs from multiangle remote sensing data. *Remote Sens. Environ.* 63:155–165.

Baldwin, D. G., and Emery, W. J. (1998), High resolution Earth surface features from repeat moderate resolution satellite imagery. *IEEE Trans. Geosci. Remote Sens.* 36:244–255.

Barnsley, M. J., Strahler, A. H., Morris, K. P., and Muller, J-P. (1994), Sampling the surface bidirectional reflectance distribution function (BRDF): 1. Evaluation of current and future satellite sensors. *Remote Sens. Rev.* 8:271–311.

Barnsley, M. J., Hobson, P. D., Hyman, A. H., Lucht, W., Mullel, J.-P., and Strahler, A. H. (2000), Characterizing the spatial variability of broadband albedo in a semidesert environment for MODIS evaluation. *Remote Sens. Environ.* 74:58–68.

Bastin, G. N., Pickup, G., and Pearce, G. (1995), Utility of AVHRR data for land degradation assessment: a case study. *Int. J. Remote Sens.* 16:651–672.

Berthelot, B., Adam, S., Dedieu, G., Maisongrande, P., Kergoat, L., and Cabot, F. (1997), A global dataset of surface reflectances and vegetation indices derived from AVHRR/GVI time series for 1989–1990: The LAnd SUrface Reflectances (LASUR) data. In *Physical Measurements and Signatures in Remote Sensing, Proceedings of the ISPRS Conference* (G. Guyot and T. Phulpin, Eds.), Courcheval, France, 7–11 April.

Brown de Colstoun, E. C., Vermote, E. R., Walthall, C. L., Cialella, A. T., Halthore, R. N., and Irons, J. R. (1996), Variability of BRDF with land cover type for the West Central HAPEX-Sahel Super Site. In *Proceedings of the IGARSS Conference 1996*, Lincoln, NE.

Burgess, D. W., and Pairman, D. (1997), Bidirectional reflectance effects in NOAA AVHRR data. *Int. J. Remote Sens.* 18: 2815–2825.

Cabot, F., Qi, J., Moran, M. S., and Dedieu, G. (1994), Test of surface bidirectional reflectance models with surface measurements : results and consequences for the use of remotely-sensed data. In *Proceedings of the Sixth International Symposium on Physical Measurements and Signatures in Remote Sensing*, 17–24 January, Val d'Isère, France, ISPRS Commission VII, pp. 627–634.

Chopping, M. J. (1998a), BRDF applications in semiarid grassland monitoring with the AVHRR. In *Developing Space '98: Proceedings of the 1998 Remote Sensing Society Student Conference*, University of Oxford, Remote Sensing Society, Nottingham, 23 April, pp. 59–67.

Chopping, M. J. (1998b), The performance of linear semi-empirical BRDF models in a semi-arid grassland biome. In *Proceedings of the Remote Sensing Society Annual Conference 1998: Developing International Connections*, Greenwich, United Kingdom, Remote Sensing Society, Nottingham, 9–11 September, pp. 568–574.

Chopping, M. J. (1998c), Linear semi-empirical kernel-driven bidirectional reflectance distribution function models in monitoring semi-arid grasslands from space, Ph.D. thesis, University of Nottingham, October (http://hydrolab.arsusda.gov/~chopping/thesis.html) (unpublished).

Chopping, M. J. (1999), Comment on "A simple method to account for off-nadir-scattering in the NOAA/NASA Pathfinder AVHRR Land Data Set" by Seaquist and Olsson [*Int. J. Remote Sens.* 20:815–822]. *Int. J. Remote Sens.* 19:7.

Cihlar, J., Manak, D., and Voisin, N. (1994a), AVHRR bidirectional reflectance effects and compositing. *Remote Sens. Environ.* 48:77–88.

Cihlar, J., Manak, D., and D'Iorio, M. (1994b), Evaluation of compositing algorithms for AVHRR data over land. *IEEE Trans. Geosci. Remote Sens.* 32:427–437.

Gallo, K., and Huang, A. (1998), Evaluation of the NDVI and sensor zenith angle values associated with the Global Land AVHRR 1-km data set. *Int. J. Remote Sens.* 19:527–533.

Goetz, S. J. (1997), Multi-sensor analysis of NDVI, surface temperature and biophysical variables at a mixed grassland site. *Int. J. Remote Sens.* 18:71–94.

Goward, S. N., Markham, B., Dye, D.G., Dulaney, W., and Yang, J. (1991), Normalized difference vegetation index measurements from the Advanced Very High Resolution Radiometer. *Remote Sens. Environ.* 35:257–277.

Goward, S. N., Dye, D. G., Turner, S., and Yang, J. (1993), Objective assessment of the NOAA global vegetation index data product. *Int. J. Remote Sens.* 14:3365–3394.

Holben, B. N. (1986), Characteristics of maximum-value composite images from temporal AVHRR data. *Int. J. Remote Sens.* 7:1417–1434.

Holben, B. N., Eck, T. F., Slutsker, I., et al. (1998), AERONET—a federated instrument network and data archive for aerosol characterization. *Remote Sens. Environ.* 66:1–16.

Hu, B., Lucht, W., and Strahler, A. H. (1999), The interrelationship of atmospheric correction of reflectances and surface BRDF retrieval: a sensitivity study. *IEEE Trans. Geosci. Remote Sens.* 37:724–738.

Huete, A. R., Liu, H., de Lira, G. R., Batchily, K., and Escadafal, R. (1994), A soil color index to adjust for soil and litter noise in vegetation index imagery of arid regions. In *Surface and Atmosphere Remote Sensing : Technologies, Data Analysis and Interpretation, Proceedings of the 1994 International Geoscience and Remote Sensing Symposium (IGARSS)*, Jet Propulsion Laboratory, California Institute of Technology, Pasadena, CA, 8–12 August.

Hyman, A. H., and Wanner, W. (1997), Relationships between semi-empirical BRDF model parameters and land cover type. In *Developing Space '97, Proceedings of the 1997 Remote Sensing Society Annual Student Meeting*, University College London, Remote Sensing Society, Nottingham, 17 April, pp. 30–35.

Hyman, A. H., Lucht, W., Barnsley, M. J., Hobson, P., Muller, J-P., and Strahler, A. H. (1998), Investigation of the spatial variability of albedo during the Grassland PROVE '97 Jornada Field Campaign. In *Proceedings of the Remote Sensing Society Annual Conference 1998: Developing International Connections*, Greenwich, United Kingdom, Remote Sensing Society, Nottingham, 9–11 September.

Jupp, D. L. B., McDonald, E. R., Harrison, B. A., Li, X., Strahler, A. H., and Woodcock, C. E. (1994), Prospects for mapping canopy structure using geometric-optical models. In *Proceedings of the 7th Australasian Remote Sensing Conference*, Melbourne, Australia, 1–4 March.

Kalluri, S. N. V., Zhang, Z., Liang, S., JaJa, J., and Townshend, J. R. G. (1997), Retrieval of bidirectional reflectance distribution function (BRDF) at continental scales from AVHRR data using high performance computing. *IGARSS 1997*:174–176.

Kremer, R. G., and Running, S. W. (1993), Community type

differentiation using NOAA/AVHRR data within a sagebrush steppe ecosystem. *Remote Sens. Environ.* 46:311–318.

Kwiatowska, E. (1995), Hybrid neural network system for cloud classification from satellite images. *Proceedings of the Remote Sensing Society One Day Student Meeting* (D. S. Boyd and M. C. Perrin, Eds.), 29 March, Department of Geography, University of Leicester, United Kingdom.

Lacaze, R., and Roujean, J-L. (1997), Cartographie des paramètres de surface utiles au climat à partir des données multiangulaires POLDER pendant HAPEX-Sahel. In *Physical Measurements and Signatures in Remote Sensing, Proceedings of the ISPRS Conference* (G. Guyot and T. Phulpin, Eds.), Courcheval, France, 7–11 April.

Leroy, M., and Bréon, F.-M. (1996), Angular signatures of surface reflectances from airborne POLDER data. *Remote Sens. Environ.* 57:97–107.

Leroy, M., and Roujean, J-L. (1994), Sun and view angle corrections on reflectance derived from NOAA AVHRR data, *I.E.E.E. Trans. Geosc. and Remote Sens.*, 32(3):684–697.

Leroy, M, Deuzé, J. L., Bréon, F.-M., et al. (1996), Retrieval of atmospheric properties and surface bidirectional reflectances over land from POLDER/ADEOS. *J. Geophys. Res. Atmos.* 102:17,023–17,037.

Lewis P. (1996) A botanical plant modelling system for remote sensing simulation studies, Ph.D. thesis, University of London, 349 pp. (http://www.geog.ucl.ac.uk/~plewis/phd).

Lewis, P. E., and Disney, M. (1997), Examining BRDF model operation with the botanical plant modelling system. In *Proceedings of the Remote Sensing Society Annual Conference 1997: Observations and Interactions*, University of Reading, United Kingdom, 2–4 September, pp. 298–303.

Lewis, P., and Wanner, W. (1996), Progress Report: Noise sensitivity of BRDF and albedo retrieval from the Earth Observing System MODIS and MISR sensors with respect to angular sampling. In Strahler, A. H., Wanner, W., Schaaf, C. B., et al. (1996), *MODIS BRDF/Albedo Product: Algorithm Theoretical Basis Document Version 4.0*, MODIS Product ID: MOD43, November, NASA/GSFC, Greenbelt, MD, Appendix C.

Lewis, P., Disney, M. I., Barnsley, M. J., and Muller, J.-P. (1999), Deriving albedo maps for HAPEX-Sahel from ASAS data using kernel-driven BRDF models. *Hydrol. Earth Syst. Sci.*, in press.

Li, X., and Strahler, A. H. (1992), Geometric-optical bidirectional reflectance modeling of the discrete crown vegetation canopy: effect of crown shape and mutual shadowing. *IEEE Trans. Geosci. Remote Sens.* GE-30:276–292.

Loeb, N. G. (1997), In-flight calibration of NOAA AVHRR visible and near-IR bands over Greenland and Antarctica. *Int. J. Remote Sens.* 18:477–490.

Los, S. O., Tucker, C. J., and Justice, C. O. (1995), Earth Observing System—Inter-Disciplinary Science: Fourier-Adjustment, Solar zenith angle corrected, Interpolated Reconstructed (FASIR) Normalized Difference Vegetation Index (NDVI) Project, Biospheric Sciences Branch, NASA/GSFC, Greenbelt, MD ((http://daac.gsfc.nasa.gov/CAMPAIGN_DOCS/ISLSCP/DATASET_DOCUMENTS/FSR_NDVI.html).

Loveland, T. R., Merchant, J. W., Ohlen, D. O., and Brown, J. F. (1991), Development of a land-cover characteristics database for the conterminous U.S. *Photogramm. Eng. Remote Sens.* 57:1453–1463.

Marçal, A. R. S., and Wright, G. G. (1997), The use of NOAA-AVHRR "overlapping" NDVI maximum-value composites for vegetation assessment in Scotland. In *Physical Measurements and Signatures in Remote Sensing, Proceedings of the ISPRS Conference* (G. Guyot and T. Phulpin, Eds.), Courcheval, France, 7–11 April.

Meyer, D., Verstraete, M., and Pinty, B. (1995), The effect of surface anisotropy and viewing geometry on the estimation of NDVI from AVHRR. *Remote Sens. Rev.* 12:3–27.

Moody, A., and Strahler, A. H. (1994), Characteristics of composited AVHRR data and problems in their classification. *Int. J. Remote Sens.* 15:3473–3491.

Ni, W., and Li, X. (2000), A coupled vegetation–soil bidirectional reflectance model for a semiarid landscape. *Remote Sens. Environ.* 74:113–124.

O'Brien, D. M., Mitchell, R. M., Edwards, M., and Elsum. C. C., (1998), Estimation of BRDF from AVHRR short-wave channels: tests over semiarid Australian sites. *Remote Sens. Environ.* 66:71–86.

Pelgrum, H., Schmugge, T., Rango, A., Ritchie, J., and Kustas, W. (1999), Length scale analysis of surface albedo, temperature and NDVI in a desert grassland, Water Resources Research, Hydrology Laboratory, USDA-ARS, BARC-W, Beltsville MD, in press.

Privette, J. L., Eck, T. F., and Deering, D. W. (1997), Estimating spectral albedo and nadir reflectance through inversion of simple BRDF models with AVHRR/MODIS-like data. *J. Geophys.Res.* 102(D24):29,529–29,542.

Privette, J. L., Emery W. J., and Schimel, D. S. (1996), Inversion of a vegetation reflectance model with NOAA AVHRR data. *Remote Sens. Environ.* 58:187–200.

Privette, J. L. and Vermote, E. F. (1995), Fitting remote sensing data with linear bidirectional reflectance models. In *Proceedings of the SPIE Symposium on Satellite Remote Sensing II, Session on Global Process Monitoring*, Paris, 25–28 September, pp. 172–179.

Qin, W., and Gerstl, S. A. W. (2000), 3-D scene modeling of semidesert vegetation cover and its radiation régime. *Remote Sens. Environ.* 74:145–162.

Rahman, H. (1996), Atmospheric optical depth and water vapour effects on the angular characteristics of surface reflectance in NOAA AVHRR. *Int. J. Remote Sens.* 17:2981–2999.

Rahman, H., and Dedieu, G. (1994), SMAC: A simplified method for the atmospheric correction of satellite measurements in the solar spectrum. *Int. J. Remote Sens.* 15:123–143.

Rao, C. R. N., and Chen, J. (1993), Calibration of the visible and near-infrared channels of the Advanced Very High Resolution Radiometer (AVHRR) after launch. In *Proceedings of the SPIE Conference of Recent Advances in Sensors, Radiometric Calibration and Processing of Remotely Sensed Data*, International Society for Optical Engineering, Bellingham, WA, pp. 56–66.

Rao, C. R. N., and Chen, J. (1996), Post-launch calibration of the visible and near-infrared channels of the Advanced Very High Resolution Radiometer on the NOAA-14 spacecraft. *Int. J. Remote Sens.* 17:2743–2847.

Rao, C. R. N., and Chen, J. (1999), Revised post-launch calibration of Channels 1 and 2 of the Advanced Very High Resolution Radiometer on board the NOAA-14 spacecraft, NOAA-NESDIS Office of Research and Applications, Washington, DC (http://psbsgi1.nesdis.noaa.gov:8080/EBB/ml/niccal1.html).

Ross, J. K. (1981), *The Radiation Regime and Architecture of Plant Stands*, Dr. W. Junk Publishers, The Hague, 392 pp.

Roujean, J.-L., Leroy, M., Podaire, A., and Deschamps, P.-Y. (1992a), Evidence of surface reflectance bidirectional effects from a NOAA/AVHRR multi-temporal data set. *Int. J. Remote Sens.* 13:685–698.

Roujean, J.-L., Leroy, M., and Deschamps, P.-Y. (1992b), A bidirectional reflectance model of the Earth's surface for the correction of remote sensing data. *J. Geophys. Res.* 97(D18): 20,455–20,468.

Simpson, J. J., and Stitt, J. R. (1998), A Procedure for the detection and removal of cloud shadow from AVHRR data over land. *IEEE Trans. Geosci. Remote Sens.* 36:880–897.

Stoms, D. M., Bueno, M. J., and Davis, F. W. (1997), Viewing geometry of AVHRR image composites derived using multiple criteria. *Photogramm. Eng. Remote Sens.* 63:681–689.

Stowe, L. L., Maclain, E. P., Arey, R., e al. (1991), Global distribution of cloud cover derived from NOAA/AVHRR operational satellite data. *Adv. Space Res.* 3:51–54.

Strahler, A. H., Wanner, W., Schaaf, C. B., et al. (1996), *MODIS BRDF/Albedo Product: Algorithm Theoretical Basis Document Version 4.0*, MODIS Product ID: MOD43, November, NASA/GSFC, Greenbelt, MD, 252 pp.

Vermote, E., Tanré, D., Deuze, J. L., Herman, M., and Morcrette, J. J. (1997), Second Simulation of the Satellite Signal in the Solar Spectrum (6S): an overview. *IEEE Trans. Geosci. Remote Sens.* 35:675–686.

Vives Ruiz de Lope, E., and Lewis, P. E. (1997), Monitoring land surface dynamics in the HAPEX Sahel area using kernel driven BRDF models and AVHRR data. In *Physical Measurements and Signatures in Remote Sensing, Proceedings of the ISPRS Conference* (G. Guyot and T. Phulpin, Eds.), Courcheval, France, 7–11 April.

Walthall, C. L., Norman, J. M., Welles, J. M., Campbell, G., and Blad, B. L. (1985), Simple equation to approximate the bidirectional reflectance from vegetative canopies and bare surfaces. *Appl. Opt.* 24:383–387.

Wanner, W., Li, X., and Strahler, A. H. (1995), On the derivation of kernels for kernel-driven models of bidirectional reflectance. *J. Geophys. Res.* 100:21,077–21,090.

Wu, A., Li, Z., and Cihlar, J. (1995), Effects of land cover type and greenness on Advanced Very High Resolution Radiometer bidirectional reflectances: analysis and removal. *J. Geophys. Res.* 100(D5):9197–9192.

Zhang, Z., Kalluri, S. N. V., JaJa, J., Liang, S., and Townshend, J. R. G. (1998), Models and high-performance algorithms for global BRDF retrieval. *IEEE Comput Sci Eng.* 5(4):16–29.

Zhu, Z.-L., and Yang, L. (1996), Characteristics of the 1-km AVHRR data set for North America. *Int. J. Remote Sens.* 17:1915–1924.